A Study on HL-LHC Beam-Beam Resonances Using a Lie Algebraic Weak-Strong Model

by

Yi Lin (Kyle) Gao
B.Math., University of Waterloo, 2017

A Thesis Submitted in Partial Fulfillment of the
Requirements for the Degree of

MASTER OF SCIENCE

in the Department of Physics and Astronomy

A Study on HL-LHC Beam-Beam Resonances Using a Lie Algebraic Weak-Strong Model

by

Yi Lin (Kyle) Gao
B.Math., University of Waterloo, 2017

Supervisory Committee

Dr. S. Koscielniak, Co-Supervisor
(Department of Physics and Astronomy)

Dr. D. Karlen, Co-Supervisor
(Department of Physics and Astronomy)

ABSTRACT

This thesis studies the resonances driven by beam-beam interactions in the planned High Luminosity upgrade to the Large Hadron Collider (HL-LHC) using a Lie algebraic formalism. With the suggested magnetic lattice for the HL-LHC, using the accelerator code MadX, bunch data (containing information such as shape, phase advance, and bunch separation) for 70 bunches over the two interaction regions (IRs), ATLAS and CMS, was computed. These data are used to create a 70 impulse beam-beam Weak-Strong model combining both long-range and head-on interactions. An effective Hamiltonian was derived for the system. The effective Hamiltonian and a width formula derived in the thesis are used to analyze the system in betatron frequency space. As algebraically derived in this thesis, resonances of order q can be removed by phase-shifting both vertical and horizontal phase advances between interaction points by $\frac{\pi}{q}$. Namely, the 16th order resonances close to the proposed working point of $(62.31, 60.32)$ can be weakened by phase advances close to $\frac{\pi}{16}$. This is reflected in frequency space plots of the effective Hamiltonian and of the width formula. Resonances are significantly weakened if phase advances are within 10^{-3} of the ideal ones for resonance cancellation; the phasing needs not be exact. The effect of crossing angle was briefly investigated; according to the effective Hamiltonian and width formula, beam-beam resonances cannot be significantly improved by increasing the tentative crossing angle of 590 μrad. However, decreasing the crossing angle significantly strengthens the resonances of the system. A new working point (0.475,0.485) suggested from a study by another author was investigated; it lies away from dangerous resonances according to the tools used in this thesis, and should be investigated further.

Table of Contents

List of Figures

1 Introduction

1.1 High-Luminosity LHC

The Large Hadron Collider (LHC), with a circumference of 27 km, designed for a collision energy of 14 TeV, is the world's largest and most powerful particle accelerator. With the discovery of the Higgs boson in 2012, the LHC constantly probes the frontier of particle physics.
The High Luminosity-LHC (HL-LHC) project, expected to be operational in 2026, aims to increase the luminosity of the LHC by potentially a factor of 10. This increase in luminosity, and the resulting increase in particle production rate, will allow for a more detailed study of the more exotic particles produced at the LHC. In particular, the HL-LHC upgrade is expected to produce at least 15 million Higgs bosons per year, triple the amount produced in 2017. However, beam-beam effects, which describe the physics of two beams passing each other at certain locations around the collider, are known to be a limiting factor [1][2].

1.2 Beam-beam effects and resonances

The LHC is a hadron synchronton, a fixed orbit particle accelerator which uses magnetic fields to bend particle beams; the fields are synchronized to the increase in particle momentum (and therefore rigidity).

In most places around the synchrotron, the transverse motion of the beam can be approximated by linear optics and quasi-harmonic (betatron) motion about the reference orbit. However, in certain interaction regions (IRs), around interaction points (IPs), non-linear effects due to beam-beam become non-negligible. These interaction points host experiments such as ATLAS and CMS.

With the increase in luminosity planned for the HL-LHC, the modelling of these effects become ever more important. Namely, the beam-beam interactions, which will be explained in section 3, can become resonant with the transverse quasi-harmonic motion of the beams.

1.3 An analytic model based on Lie algebra

A natural language to study non-linear systems is the Lie algebraic formulation of Hamiltonian mechanics. In this formalism, (symplectic) maps are abstracted to Lie

groups, and equations of motions are abstracted to their Lie algebras. This allows for the study of non-linear effects in a language that is analogous to matrix algebra. This formalism has the geometry of Hamiltonian phase space [1], and its conservation laws, naturally built in.

Alex J. Dragt [3], introduced and popularized the "Lie operator formalism" to the field of accelerator physics. By introducing simple notations, and distilling the essence of symplectic geometry to its algebra, he constructed a formalism now favored for the study of non-linear dynamics in accelerator physics. This thesis will use the same conventions as Dragt, with the exception that here, $\{,\}$ corresponds to Poisson bracket, and $[,]$ corresponds to commutator or other Lie brackets, depending on context.

1.4 Object of study and goal

The goal of this thesis is to study the beam-beam effect and its resonances using "Lie algebra formalism", in order distinguish stable regions in phase space from unstable ones due to beam-beam effects.

This type of study is usually done by performing a frequency space analysis using "tracking". In this context, "tracking" means solving for the motion of a huge number of particle with different initial conditions, by tracking their long time stability for millions of turns and by quantifying stability in frequency space.

The computational demand can be so large that these simulations are often run on the distributed computing network (such as BOINC [4]), or in parallel on GPUs [5].

Recent development [6] show that the "Lie algebra method" allows for a less computationally intensive analysis of beam-beam effects coupled to betatron motion.

1.5 Outline of thesis

This thesis studies beam-beam interactions and their resonances using the model of many beam-beam impulses coupled to a harmonic oscillator like linear one-turn map using Lie algebraic methods (Section 4). An effective Hamiltonian for a one-turn map coupled to 70 beam-beam impulses is computed (Eq.107) and plotted (Figure 14) in frequency space to study resonances of this system. The model uses real HL-LHC

[1] Phase space is the space of canonical positions and momenta

bunch data. In this thesis, "bunch data" refer to the normalized separations, phase advances, and shapes of bunches in interaction regions, calculated from the HL-LHC magnet lattice using MadX (Appendix A). The effective Hamiltonian is shown to agree with numerical tracking away from resonance (Section 6.1). A width formula is developed for resonance lines (124). The theory also predicts the possibility of weakening, or even removing resonances of certain orders using appropriate phasing of beam-beam impulses (Section 6.2). This is verified against the effective Hamiltonian and the width formula. These tools are used to study the resonances close to the suggested working point of the HL-LHC as well as a new working point suggested by a previous study by Furuseth [7]. The effects of changing separations (crossing angles) are also studied (Section 6.5).

2 Hamiltonian dynamics and linear beam optics

This section introduces the reader to basic accelerator physics in the context of classical Hamiltonian mechanics. The section first introduces linear accelerator optics, and transitions to perturbations.

2.1 Variational principle

Classically, Hamiltonian mechanics has been thought of as a reformulation of Lagrangian mechanics[2]. Even without use of the Legendre transform, Hamilton's equations are usually derived from the variational principle. This is done by optimizing the Lagrangian action, written in terms of phase space variables (Q, P) instead of Lagrangian variables. That is to say, using variational methods, find a curve $(..., Q_i(t), ..., P_j(t), ...)$ optimizing the action S:

$$S = \int \sum P_i dQ_i - H dt. \tag{1}$$

$(Q's, P's)$ are canonical positions and momenta, they may or may not correspond to physical ones.
The solutions are curves satisfying Hamilton's equations;

$$\frac{dQ_i}{dt} = \frac{\partial H}{\partial P_i}, \quad \frac{dP_i}{dt} = -\frac{\partial H}{\partial Q_i}. \tag{2}$$

By defining $P_t = -H, Q_t = t$, $P_j = -H_j, Q_j = q_j$,

$$S = \int \sum_{i \neq j} P_i dQ_i + P_t dQ_t - H_j dq_j. \tag{3}$$

Since the extremum does not depend on parameterization, (3) tells us that any one of the momenta $-P_j$ can be used as a Hamiltonian, and its corresponding canonical position as independent variable. One finds that Hamilton's equations become

$$\frac{dQ_i}{dq_j} = \frac{\partial H_j}{\partial P_i}, \quad \frac{dP_i}{dq_j} = -\frac{\partial H_j}{\partial Q_i}, \quad \frac{dQ_t}{dq_j} = \frac{\partial H_j}{\partial P_t}, \quad \frac{dP_t}{dq_j} = -\frac{\partial H_j}{\partial Q_t}. \tag{4}$$

The relativistic electromagnetic Hamiltonian for a single particle of mass m expe-

[2]Hamilton 1833, Lagrange 1788

riencing a scalar potential Φ and vector potential $\vec{A}$ can be written as

$$H_t = e\Phi + c\sqrt{m^2c^2 + (P_x - eA_x)^2 + (P_y - eA_y)^2 + (P_z - eA_z)^2} \tag{5}$$

where P's are canonical momenta, and c is the speed of light.

By changing independent coordinates to $s = z$, the Hamiltonian becomes

$$H_s = -eA_s - \sqrt{-m^2c^2 - (P_x - eA_x)^2 - (P_y - eA_y)^2 + (\frac{E - q\Phi}{c})^2}. \tag{6}$$

The beauty of phase space geometry is hinted at from equations (1) (2); canonical positions and momenta are seemingly on equal footing. This hints at the possibility that Hamiltonian mechanics can be approached geometrically. This will be emphasized in the alternate geometric formulation developed mid-late 20th century, introduced in section 4.

Linear magnets (dipoles and quadrupoles) have dominant potential terms of order ≤ 2. The resulting equations of motion are linear. The problem is then simple optical (ray transfer) matrix operations. This is the foundation of many tracking codes such as MadX.

2.2 Coordinate system

While modelling transverse motion, accelerator physicists are interested in deviations from a reference trajectory (the ideal trajectory of a particle through the centre of all magnetic elements).

This is mathematically defined by the Frenet-Serret coordinate system following the reference orbit. When the reference orbit lies entirely in a plane, the Frenet-Serret coordinates simplifies to:

- $\hat{s}$ the local tangent unit vector to the reference orbit, with s measuring distance along the trajectory
- $\hat{x}$ the horizontal normal unit vector, with x measuring horizontal deviation from reference trajectory, and $\frac{\partial}{\partial x}$ containing a local curvature factor $h = 1/\rho$
- $\hat{y}$ the vertical normal unit vector, defined in a right handed coordinate system as $\hat{y} = \hat{s} \times \hat{x}$, with y measuring vertical deviation from reference trajectory

For circular accelerators, in sections with constant local curvature lying in a plane, it is sufficient to map a shifted cylindrical coordinate system's unit vectors (ρ, θ, y) at a fixed radius ρ onto a locally Cartesian one (x, y, s) by mapping $\hat{\theta} \to -\hat{s}$, $\hat{\rho} \to \hat{x}$, $\hat{y} \to \hat{y}$. In practice, in most circular accelerators, it suffices to construct the coordinate system pieces by gluing local Cartesian and local cylindrical coordinate systems.

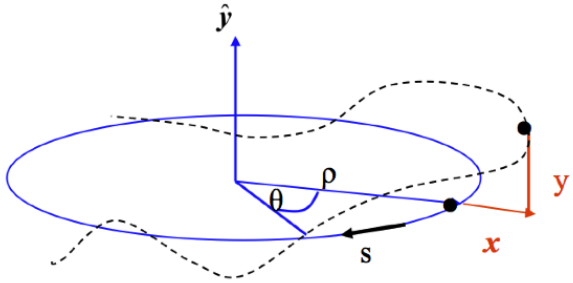

Figure 1: Diagram of right-handed Frenet-Serret coordinate system as a cylindrical coordinate system (Figure 3 in [8])

2.3 Linear beam optics

Magnetic fields are used to control transverse deviations from reference orbits and effects caused by such deviations. In this context, consider the Lorentz force, $F = e(v \times B)$. It is standard to use the longitudinal coordinate s as independent variable; let $\dot{x}$ denote total time derivative, and x' denote total s derivative.

$$\begin{aligned} \ddot{x} &= \frac{e}{m}(\dot{y}B_s - \dot{s}B_y). \\ \ddot{y} &= -\frac{e}{m}(\dot{x}B_s - \dot{s}B_x). \end{aligned} \tag{7}$$

It can be shown[9] in a fixed Cartesian coordinate that (7) can be written as:

$$x'' = \frac{v}{\dot{s}}\frac{e}{p}(y'B_s - (1 + x'^2)B_y + y'x'B_x). \tag{8}$$

$$y'' = -\frac{v}{\dot{s}}\frac{e}{p}(x'B_s - (1 + y'^2)B_y + y'x'B_y). \tag{9}$$

The particle's motion in the transverse (x, y) plane is called betatron motion. Let us assume there are no solenoidal fields.

Maxwell's equations in the vacuum of a beam pipe are:

$$\begin{aligned} \boldsymbol{\nabla} \cdot \vec{B} &= 0. \\ \boldsymbol{\nabla} \times \vec{B} &= 0. \end{aligned} \tag{10}$$

This implies that that $\vec{B}$ can be written as both the curl of some vector potential $\vec{A}$, and the gradient of some scalar potential V.

$$\begin{aligned} \vec{B} &= \boldsymbol{\nabla} \times \vec{A}. \\ \vec{B} &= -\boldsymbol{\nabla}\, V. \end{aligned} \tag{11}$$

By demanding the $\vec{B}$ fields be constant along $\hat{s}$ inside the magnet, the vector potential only requires A_s component. Using (11), we obtain the following constraint for the field expansion:

$$\begin{aligned} B_x &= -\frac{\partial V}{\partial x} = \frac{\partial A_S}{\partial y}. \\ B_y &= -\frac{\partial V}{\partial y} = -\frac{\partial A_S}{\partial x}. \end{aligned} \tag{12}$$

The above constraint is the Cauchy Riemann equation [10], which is the analyticity condition for the complex function $A_s(x,y) - iV(x,y)$. Expanding the potentials as a complex analytic function:

$$A_s(x,y) - iV(x,y) = \sum_n (a_n + ib_n)(x+iy)^n. \tag{13}$$

From the expansion:

$$\begin{aligned} A_s &= Re[\sum_n (a_n + ib_n)(x+iy)^n] \\ &= a_0 + a_1 x - b_1 y + a_2(x^2 - y^2) - b_2(2xy) + O(z^3), \quad z = x + iy. \end{aligned} \tag{14}$$

From here, it is easy to identify multipole terms.

The multipole expansion can also be expressed in polar coordinates. By substi-

tuting $(x+iy)^n = r^n e^{in\theta}$, and using Euler's identity,

$$A_s = Re[\sum_n (a_n + ib_n) r^n e^{in\theta}] = a_0 + \sum_{n=1}^{\infty} r^n (a_n \cos(n\theta) - b_n \sin(n\theta)). \tag{15}$$

2.3.1 Magnetic dipole

A dipole magnet generates constant field [9]. From Ampere's law, with gap height h and current-turn nI:

$$B_y = B_0 = \frac{\mu_0 nI}{h}. \tag{16}$$

We can identify $-a_1$ in the vector potential (14) term to be the dipole field B_0.

Dipole magnets bend charged particles. Using the uniform circular motion equation, the bending radius ρ depends on the particle's momentum:

$$\rho = \frac{p}{eB_0}. \tag{17}$$

Hence the magnetic rigidity:

$$B_0 \rho = \frac{p}{e}. \tag{18}$$

Dipole magnets are used to bend the beam. Particles that differ in momentum have different bending radius. Around the ring, it is described by the dispersion function, which is to be addressed in section 2.5.

2.3.2 Magnetic quadrupole

The poles of a quadrupole magnet are hyperbolic in shape. The field is a linear function of distance from the axis. Let G be the field gradient, the B field can be written as

$$\begin{aligned} B_x &= Gy. \\ B_y &= Gx. \end{aligned} \tag{19}$$

The vector potential is chosen to be $A_s = -\frac{K}{2}(x^2 - y^2)$, $A_x = A_y = 0$, where $K = \frac{eG}{p}$.

Quadrupoles are used to focus the beam. A quadrupole which focuses vertically, defocuses horizontally; and vice-versa. The principle of Strong Focusing, to be elaborated in a later section, uses alternating focusing and defocusing quadrupoles to generate a net focusing effect.

2.3.3 Hill's equation

Hill's equation (20) is a second order linear ordinary differential equation,

$$\frac{dy^2}{ds^2} + f(s)y = 0 \tag{20}$$

where $f(s)$ is a periodic function, or a function defined on a fixed finite interval in s (a single period).

It governs systems such as propagation through periodically loaded transmission lines, the wave-function of an electron in a periodic lattice, and particle orbits in an accelerator with a periodic lattice [11].

In the case of context of linear beam optics, $f(s)$ is a piece-wise constant function, in which case (20) takes a simple form.

Being a second order linear ordinary differential equation, it admits a space of solutions such that two linearly independent solutions can be chosen to construct the others. It is standard to choose one of the two solutions to be $C(s)$, a cosine like function, with $C(0) = 1$, $C'(0) = 0$. The other one is chosen to be $S(s)$, a sine like function, with $S(0) = 0$, $S'(0) = 1$.

The general solution is a linear combination of the two; this can be written as a transfer matrix multiplication:

$$\begin{bmatrix} y(s) \\ y'(s) \end{bmatrix} = \begin{bmatrix} C(s) & S(s) \\ C'(s) & S'(s) \end{bmatrix} \begin{bmatrix} y(0) \\ y'(0) \end{bmatrix}. \tag{21}$$

Another common way to represent the solution is

$$y = \sqrt{\epsilon\beta(s)}\cos(\phi(s) + \phi_0). \tag{22}$$

2.3.4 Transfer matrices

The equations of motion of a charged particle passing through a dipole or a quadrupole may be written as:

$$x'' + K_x(s)x = \frac{1}{\rho}\frac{\Delta p}{p}. \tag{23}$$

$$y'' - K_y(s)y = 0. \tag{24}$$

$K(s)$ is piece-wise constant. The $\frac{\Delta p}{p}$ term is relative momentum deviation, which results in orbit dispersion. Let G be the magnetic field gradient. Let p be the longitudinal momentum of the reference particle and e be its charge.

For a horizontally focusing quadrupole, $K(s) = k = \frac{G}{ep} > 0$,

$$\begin{bmatrix} x(s) \\ x'(s) \end{bmatrix} = \begin{bmatrix} \cos\left(\sqrt{|k|}s\right) & \frac{\sin\left(\sqrt{|k|}s\right)}{\sqrt{|k|}} \\ -\sqrt{|k|}\sin\left(\sqrt{|k|}s\right) & \cos\left(\sqrt{|k|}s\right) \end{bmatrix} \begin{bmatrix} x(0) \\ x'(0) \end{bmatrix}. \tag{25}$$

For a horizontally defocusing quadrupole, $K(s) = k = \frac{G}{ep} < 0$

$$\begin{bmatrix} x(s) \\ x'(s) \end{bmatrix} = \begin{bmatrix} \cosh\left(\sqrt{|k|}s\right) & \frac{\sinh\left(\sqrt{|k|}s\right)}{\sqrt{|k|}} \\ \sqrt{|k|}\sinh\left(\sqrt{|k|}s\right) & \cosh\left(\sqrt{|k|}s\right) \end{bmatrix} \begin{bmatrix} x(0) \\ x'(0) \end{bmatrix}. \tag{26}$$

K=0 corresponds to a drift (unless $\frac{1}{\rho}$ is non-zero, which corresponds to a dipole),

$$\begin{bmatrix} x(s) \\ x'(s) \end{bmatrix} = \begin{bmatrix} 1 & s \\ 0 & 1 \end{bmatrix} \begin{bmatrix} x(0) \\ x'(0) \end{bmatrix}. \tag{27}$$

The focal length of a quadrupole is given by $f = \frac{1}{kL}$, where L is the magnet's length. For $f >> l$, the thin lens approximation may be used. Taking the limit as $L \to 0$, with $kL = \frac{1}{f}$, the transfer matrices in (25) and (26) can be approximated as:

$$\begin{aligned} M_f &= \begin{bmatrix} 1 & 0 \\ -\frac{1}{f} & 1 \end{bmatrix}. \\ M_d &= \begin{bmatrix} 1 & 0 \\ \frac{1}{f} & 1 \end{bmatrix}. \end{aligned} \tag{28}$$

From the equations of motion, it is clear that a quadrupole which focuses in x will defocus in y, since $k \to -k$, so $f \to -f$, and vice-versa. However, the principle of Strong Focusing shows that alternating focusing and defocusing quadrupoles will have a net focusing effect. Consider a thin focusing lens, followed by a drift and a thin defocusing lens,

$$
\begin{aligned}
M &= \begin{bmatrix} 1 & 0 \\ \frac{1}{f} & 1 \end{bmatrix} \begin{bmatrix} 1 & L \\ 0 & 1 \end{bmatrix} \begin{bmatrix} 1 & 0 \\ -\frac{1}{f} & 1 \end{bmatrix} \\
&= \begin{bmatrix} 1 + \frac{L}{f} & L \\ -\frac{L}{f^2} & 1 - \frac{L}{f} \end{bmatrix}
\end{aligned} \tag{29}
$$

where the $-L/f^2$ focusing term is negative regardless of sign of f.

It is on this Strong Focusing principle that the LHC is built. The beam optics elements are arranged in a periodic lattice structure. The most common is the FODO cell, a focusing half quadrupole, followed by drift, a defocusing quadrupole, another drift, and a final focusing half quadrupole. The LHC contains 8 arcs, each with 23 FODO cells 107 meters in length [12].

2.4 The envelope equation and Courant-Snyder parameters

In the context of betatron motion, the solutions curves can be expressed as cosine and sine functions; a parameter dependent ellipse is traced out in phase space as a function of the betatron phase. Particles with the same given amplitude but different phases will lie along the ellipse.

The general equation of an ellipse in x, x' can be written as

$$
\epsilon = \gamma x^2 + 2\alpha x x' + \beta x'^2 \tag{30}
$$

For beam optics, the coefficients are called Courant-Snyder parameters, or Twiss parameters. In this context, α, β, γ are implicit functions of the independent variable s.

The β parameter describes size, with $\sqrt{\epsilon\beta} = x_{max}$.

The α parameter describes ellipse tilt.

The γ parameter can be written as $\gamma = \frac{1+a^2}{\beta}$, with $\sqrt{\epsilon\gamma} = x'_{max}$.

The geometric emittance ϵ measures the area of the ellipse $A = \pi\epsilon$.

Courant-Snyder parameters are used in two different contexts; to describe properties of both the machine and the beam. The linear betatron motion induced by the machine is quasi-periodic; orbits trace out (as a function of phase) ellipses in phase space, the shapes and orientations of which change along the longitudinal coordinate.

These ellipses can be represented by the parameters. In this context, the parameters are properties of the lattice. For a ring, because of periodicity, the Courant-Snyder parameters are unique.

Ensembles of particles are described by statistical distributions in phase space which can be approximated by ellipses. The ellipse representing a distribution evolves like a Courant-Snyder ellipse as it travels through the accelerator. In this context, the parameters describe properties of the beam. Each beam can be described by infinitely many sets of Courant-Snyder parameters, one of which matches that of the lattice. If matched, the beam's ellipse returns to the same Courant-Snyder ellipse after each turn.

The emittance is inversely proportional to beam momentum; a normalized emittance can be introduced $\epsilon_* = \beta\gamma\epsilon$, (relativistic β and γ).

The phase space parameters have their own equations of motion. The evolution of β in particular is useful.

Writing the solutions to Hill's equation as $x(s) = \sqrt{\epsilon\beta(s)}\cos(\phi(s) + \phi_0)$, and substituting into the equations of motion, the equation of motion for β can be found:

$$\frac{1}{2}\beta\beta'' - \frac{1}{4}\beta'^2 + K(s)\beta^2 = 1. \tag{31}$$

Letting $u(s) = \sqrt{\epsilon\beta}$ be the envelope, a second order DE for the envelope may be written.

$$u'' + K(s)u - \frac{\epsilon^2}{u^3} = 0. \tag{32}$$

This non-linear equation can be solved numerically. In practice however, the envelope or the β function is found by studying the one-turn matrix at some location s,

$$M(s) = \begin{bmatrix} \cos\mu(s) + \alpha(s)\sin\mu(s) & \beta(s)\sin\mu(s) \\ -\gamma(s)\sin\mu(s) & \cos\mu(s) - \alpha(s)\sin\mu(s) \end{bmatrix}. \tag{33}$$

One then equates this symbolic matrix to the numerical one computed by multiplying transport matrices for one turn starting and ending at s.

$$M(s) = \begin{bmatrix} m_{11} & m_{12} \\ m_{21} & m_{22} \end{bmatrix}. \tag{34}$$

Then $\beta(s)$ is just given by

$$\begin{aligned} \mu(s) &= \cos^{-1}(Tr(\frac{M(s)}{2})) \\ \beta(s) &= \frac{m_{12}}{\sin\mu(s)} \end{aligned} \tag{35}$$

This is repeated at different values of s to obtain the longitudinal dependence of the envelope. The other Courant-Snyder parameters can be obtained by the same method.

One notes that this procedure can be easily extended to a 4D phase space. In absence of $x-y$ coupling, one simply constructs the 4D matrices block diagonally with the 2D matrices of $x-x'$, $y-y'$.

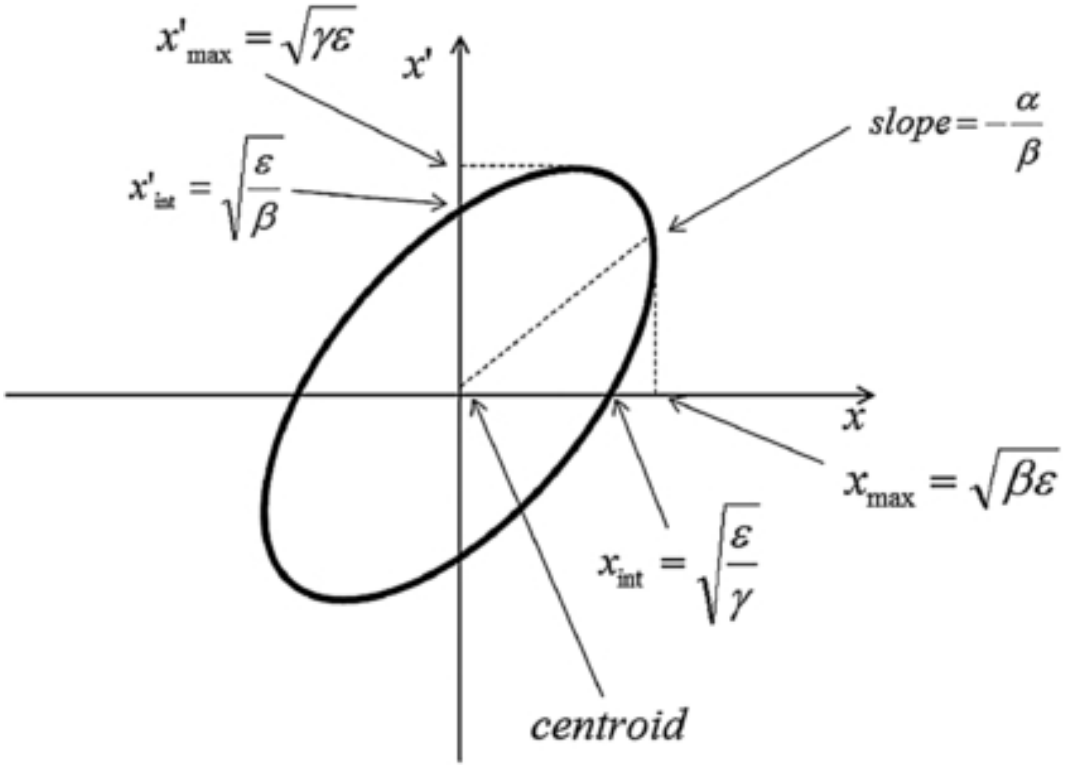

Figure 2: Courant-Snyder ellipse (Figure 2 in [13])

2.4.1 Emittance

The emittance has unit of length (angle $\times$ distance) and is a measure of phase space area. It is important to distinguish between single particle emittance, and beam

emittance. Single particle emittance refers to the geometric emittance of the phase space ellipse traced out (as a function of phase, at fixed s) by the solution to hill's equation, $x = \sqrt{\epsilon\beta(s)}\cos(\phi(s) + \phi_0)$ for the trajectory of a single particle. If we observe the turn by turn motion of a particle at the same location in s, we see that it lies on this Courant Snyder ellipse. For now, let us only consider $\sqrt{\epsilon\beta}$ to be the particle's local amplitude. Using the equation for area of ellipse, we find it to be $\frac{\pi\epsilon}{\sqrt{\gamma\beta-\alpha^2}} = \pi\epsilon$.

For the beam, consider a distribution of particle in phase space (x, x') at a fixed s. Choosing an amplitude $\sqrt{\epsilon\beta_x} = \sigma_x$ such that one standard deviation of positions x are enclosed within the ellipse. Simultaneously, we require $\sqrt{\gamma\beta_x} = \sigma_{x'}$ to enclose a standard deviation of angles x'. $\epsilon = \frac{\sigma_x^2}{\beta_x}$, gives the emittance of the beam, sometimes also denoted as ϵ_{RMS}. This can be expressed in terms of statistical moments of x and x' as $\epsilon = \sqrt{< x^2 >< x'^2 > - < xx' >^2}$.

2.5 Dispersion function

Consider (23), with non-zero momentum deviation $\frac{\Delta p}{p} = \delta$. The solution is then $x(s) = x_h(s) + \delta D(s)$, where x_h is the homogeneous solution, and D is the dispersion function which may be computed using a Green's function, and describes the dependence on δ to linear order.

For Hills type equations, D is given by [9] as

$$D(s) = S(s)\int_0^s \frac{C(s')}{\rho(s')}ds' - C(s)\int_0^s \frac{S(s')}{\rho(s')}ds'. \tag{36}$$

In practice, the result of this integral is well known for common accelerator elements (Steffan in [9]). The linear dispersion function D is included in the transfer matrix by using an additional column

$$\begin{bmatrix} R_{11} & R_{12} & D \\ R_{21} & R_{22} & D' \\ 0 & 0 & 1 \end{bmatrix} \begin{bmatrix} x_0 \\ x_0' \\ \delta \end{bmatrix} = \begin{bmatrix} x(s) \\ x'(s) \\ \delta \end{bmatrix}. \tag{37}$$

The total dispersion after multiple elements can be found via matrix multiplication.

The closed dispersion function η can also be found. The closed orbit of a one-turn map M is its stable fixed point, $M(x(s_0)) = x(s_0)$. There are numerous methods for

solving such problems in order to find the closed orbit (fixed-point iteration, Newton's method). The closed dispersion function η can be found by imposing the fixed point condition. To linear order, the analysis reduces to a matrix eigenvector equation.

$$\begin{bmatrix} \cos\mu(s) + \alpha(s)\sin\mu(s) & \beta(s)\sin\mu(s) & D(s+C) \\ -\gamma(s)\sin\mu(s) & \cos\mu(s) - \alpha(s)\sin\mu(s) & D(s+C)' \\ 0 & 0 & 1 \end{bmatrix} \begin{bmatrix} \eta \\ \eta' \\ 1 \end{bmatrix} = \begin{bmatrix} \eta \\ \eta' \\ 1 \end{bmatrix} \quad (38)$$

where C is the circumference of the ring and the matrix map is a one turn map.

Note that in general, we can have non-linear dependence on δ which give rise to higher order dispersion. For a Lie method based approach, one studies a one turn Lie map coupling the closed dispersion function η and momentum deviation δ to transverse motion.

2.6 Perturbations

2.6.1 Tune shift

In accelerator physics, the tunes $\nu_{x,y}$ are the number of betatron oscillations per revolution around the accelerator. They may also be given in radians as $\mu_{x,y}$; in this form it is also called phase advance per turn. For a Hamiltonian H, the bare (un-shifted) tunes are given by

$$\mu_{x,y} = \frac{\partial H}{\partial A}_{x,y} \quad (39)$$

where $A_x = \oint x\ dp_x$, $A_y = \oint y\ dp_y$.

Given a Hamiltonian $H_0 + V$, where H_0 is the simple harmonic oscillator and $V = \int_0^x F(x', s)dx'$ is the potential for a periodic impulse (also called a kick).

To calculate the tune shift for the whole ring,

$$\Delta\nu_{x,y} = \frac{\partial < V >}{\partial A_{x,y}}. \quad (40)$$

where $< V >$ is the average of the potential over the angles in action-angle coordinates, and over the independent angle coordinate $\theta = \frac{1}{\nu}\int_0^s \frac{ds'}{\beta s'}$.

It can be shown [14] that in action-angle coordinates, the tune shift (in 1-D) is given by

$$\Delta\nu = -\frac{1}{4\pi^2\nu\sqrt{2A}}\int d\phi \sin\phi \int d\theta \nu^2 \beta^{3/2} F(\sqrt{2A}\sin\phi, \theta). \tag{41}$$

The tune shift in general can be computed via particle tracking. The amplitude dependence of the tune shift causes an ensemble of particle to form a distribution in frequency space. The tune footprint is the 2 dimensional representation of detuning at machine bare tune caused by this amplitude dependent tune spread. It is important to minimize the tune spread, and to choose a working tune far enough away from dangerous resonance lines such that the footprint does not fall on such resonances.

2.6.2 Closed orbit distortion

Closed orbit distortion refers to effects which change the orbit of a particle on the reference orbit. The most common ones are lattice errors such as alignment and strength errors.

For the long-range beam-beam, there is another closed orbit distortion effect. When the beams are separated by a normalized distance d, a test particle at the origin of one of the beam will experience a force due to the other beam. This effect can be adjusted for by shifting the "Weak bunch coordinates" [3] and subtracting away this force.

2.6.3 Tune space and resonance

Given an integrable Hamiltonian system, an action-angle transformation is permitted. The solutions are oscillatory and form a topological n-torus [15].

Let $\nu = \frac{\mu}{2\pi}$ denote the tune of the system in cycles per turn, where μ is the tune in radians. When an integrable Hamiltonian system is perturbed, resonances may form when the tunes of the system satisfy

$$m\mu_x + n\mu_y = 2\pi q \tag{42}$$

where m, n, q are integers.

For a weak perturbation, this can be easily understood in terms of the effective Hamiltonian of the system (107), where resonances correspond to singularities. In general, not every such line is active. The active ones may not necessarily be unstable.

[3] The Weak-Strong model is explained in the next section.

The Hamiltonian of the one-turn map is as an invariant of motion, independent of the independent variable (in this case the turn index). For these type of Hamiltonian, the solution curves (orbits) lie [4] on the level surfaces of the Hamiltonian. Poincare sections [16] may be constructed, allowing the analysis of dynamical systems as maps. Far from resonance, the repeated intersection of the orbit in phase space with the Poincare section's surface lie on smooth curves. Near resonances, the topology of these curves break, and the motion becomes chaotic [17].

The solution lines of (42) is dense in the space of tunes. In theory, this means that every position in tune space is infinitesimally close to some resonance. But not all resonances are equally strong. In practice, higher order resonances contribute negligibly to chaotic behaviour. See figure 8.

In accelerator physics, non-linear effects coupled to the quasi-harmonic transverse (betatron) motion drive resonances. This effect may be studied using Guignard's analysis [18], or Lie algebra formalism [3][14]. When near resonance, the long-term stability of a particle's transverse motion is not guaranteed. This can cause a drop in dynamic aperture, the stability region in phase space.

[4] The orbits fill the space densely, by Poincare Recurrence.

3 Beam-beam interaction

The LHC collides bunches from two opposing beams. These intersect at four Interaction Points (IPs) in four out of the eight interaction regions (IRs): ATLAS, CMS, Alice, LHCb. See figure 3.

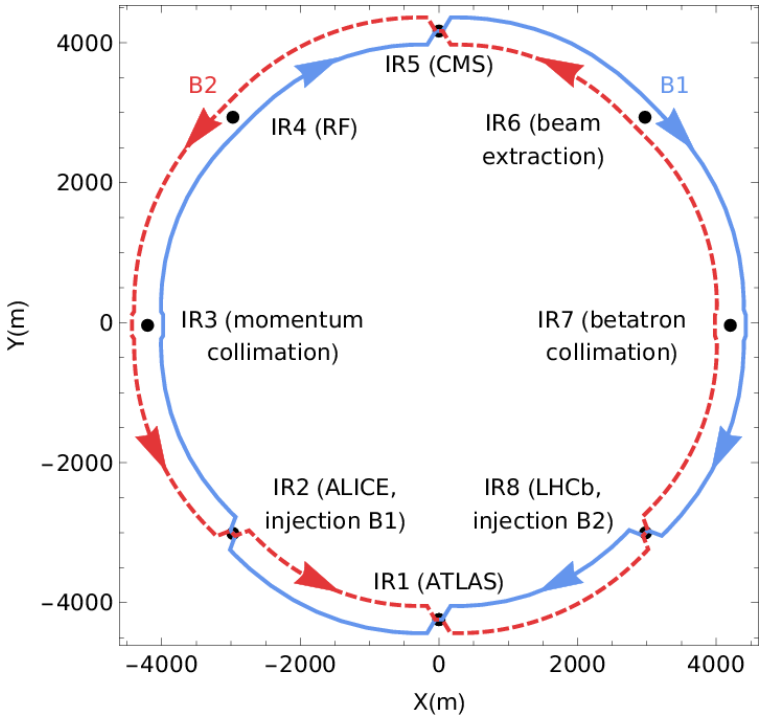

Figure 3: LHC schematic layout (Figure 1 in [19])

The increase in luminosity planned for the HL-LHC increases the contribution of the beam-beam effect to the overall non-linearity of the system.

3.1 Transverse impulse due to a charge distribution

The Weak-Strong model treats the "Weak beam's" bunches as being composed of test particles, which experience beam-beam impulses (also called beam-beam kicks) caused by the Strong bunches in the "Strong beam". This does not mean that one beam is stronger than the other, only that coherent effects between the two beams are ignored.

Consider a cylindrically symmetric charge distribution which has Gaussian drop off as function of cylindrical radius r. Let the charge distribution be also Gaussian

in the longitudinal direction.

Suppose the charge distribution moves in the longitudinal direction. The resulting electric and magnetic fields can be computed by a Lorenz transformation. The resulting effect is a pancaking of the rest frame (charge distribution frame) electric field in the boosted frame (lab frame). In the relativistic limit, the field becomes strictly transverse; the longitudinal dependence can be ignored (trivial to integrate out). The beam-beam interaction is treated as an impulse.

A general three dimensional round beam charge distribution takes the form of

$$\rho = \frac{ne}{\sigma_r^2 \sigma_z (2\pi)^{3/2}} e^{-\frac{r^2}{2\sigma_r^2} - \frac{s^2}{2\sigma_s^2}}. \tag{43}$$

The net contribution of the longitudinal component of the force experienced by a test particle in the counter rotating "weak beam" of charge e moving at velocity v in the field generated by this "strong beam" charge distribution is zero. The transverse component of the force is [20]

$$F_r(r,s,t) = \frac{ne^2(1+\beta^2)}{(2\pi)^{3/2}\epsilon_0 r}(1 - e^{-\frac{r^2}{2\sigma^2}}) e^{-\frac{(s+vt)^2}{2\sigma_s^2}}. \tag{44}$$

The transverse impulse generated by this force is

$$\Delta r' = \frac{1}{mc\beta\gamma}\int_{-\infty}^{\infty} F_r dt = \frac{2ne^2}{4\pi\epsilon_0 \gamma mc^2 r}(1 - e^{\frac{-r^2}{2\sigma^2}}). \tag{45}$$

Given that the longitudinal dependence is integrated out, a strictly transverse approach may be taken to arrive at the same result.

The transverse charge distribution is [20]

$$\rho = \frac{ne}{\sigma^2(2\pi)} e^{-\frac{r^2}{2\sigma^2}}. \tag{46}$$

Derived by Houssais [21], as cited in [22], the electric potential may be written as

$$\Phi = \frac{ne}{4\pi\epsilon_0}\int_0^{\infty} \frac{e^{-\frac{r^2}{2\sigma^2+q}}}{(2\sigma^2+q)} dq \tag{47}$$

where σ denotes the "Strong Bunch" distribution's standard deviation. This is the conventional form for beam-beam interactions [23].

The magnetic fields are related to the electric fields by the equations

$$\begin{aligned} B_y &= -\beta E_x/c. \\ B_x &= \beta E_y/c. \end{aligned} \tag{48}$$

This results in a radial force due to the fields E_r and B_ϕ. For two beams of the same charge,

$$F_r(r) = \frac{ne^2(1+\beta^2)}{2\pi\epsilon_0 r}(1 - e^{-\frac{r^2}{2\sigma^2}}). \tag{49}$$

The longitudinal dependence can be restored, resulting in (44), and then integrated over to generate an impulse.

The beam-beam parameter ξ, which is a measure of interaction strength, is equal to the tune shift for particle of zero amplitude during head-on beam-beam interactions. It is defined as

$$\xi = \frac{nr_0\beta_{cs}}{4\pi\gamma\sigma^2} \tag{50}$$

where $r_o = \frac{e^2}{4\pi\epsilon_0 mc^2}$ is the classical particle radius.

The Hamiltonian of an impulse is the integral of the impulse over the independent variable. There is no kinetic term.

Normalizing the Hamiltonian by $\frac{nr_0}{\gamma}$ and after a change of variable (see section 3.3), the Hamiltonian may be written in the form of

$$H = \int_0^P (1 - e^{-tP})\frac{dt}{t} \tag{51}$$

where $p = \frac{r^2}{\sigma^2}$. This may be written using the Euler Gamma function [24].

$$H = \gamma + \Gamma_0(P) + \ln(P). \tag{52}$$

Gauss's Law may be used to arrive at the same result for this highly symmetrical case.

3.2 2D Weak-Strong long-range model

The beam-beam effect will be treated using a 2D Weak-Strong long-range model. The bunches are elliptical 2D Gaussian distributions with unequal σ_x, σ_y. The beams are separated by a distance $D(s) = \sqrt{D_x^2(s) + D_y^2(s)}$, which goes to zero at the interaction point. D_x and D_y are the horizontal and vertical planes respectively.

In the interaction regions, the separation distances decrease linearly. This distance, when normalized by the beam's emmitance, is constant (except at the IP) in a ≈ 60 meters region around the interaction point [25]. The longitudinal bunch separation is around 25 ns, during which no significant change occur in transverse dynamics. Bunches in the opposing weak and strong beam come into close proximity each 12.5 ns.

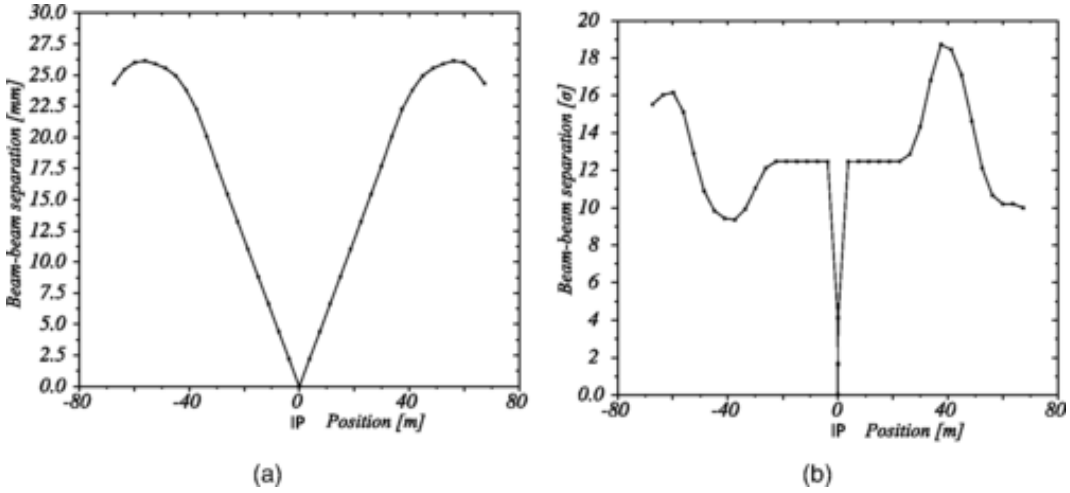

Figure 4: Beam-beam separation in standard(left) and normalized(right) coordinates. (Figure 3 in [25])

3.2.1 Weak-Strong vs Strong-Strong model

The treatment is mirrored when modelling the bunches in the other beam, as the beta functions have the symmetries $\beta_x^1 = \beta_y^2$, $\beta_x^L = \beta_y^R$ [25].

The Strong-Strong model treats both beams as affecting each other; the effects caused by this coupling are modelled. This problem is much more complicated and requires an entirely different set of approximations, namely various field discretizations not used in Weak-Strong models. Due to these additional approximations, the Strong-Strong model is not necessarily a more accurate model in the Weak-Strong regime.

There are strictly Strong-Strong effects which are invisible to the Weak-Strong model such as certain coupled oscillation modes due to mutual perturbation [26]. These coherent modes are important in the analysis of impedance driven instabilities [27]. There are various work using the Strong-Strong model [28][29].

3.2.2 Head-on interactions

The head on model treats the beam-beam interaction as occurring at the intersection point of the two beams; both beams share a common axis at the interaction point.

The potential and the Hamiltonian in this case is rotationally symmetric for round beams, and has elliptical symmetry for elliptical beams. The Fourier coefficients (3.3) are faster to compute in these cases. Furthermore, the odd coefficients are zero since the potential is symmetric about the origin. It is important to note that the Fourier coefficients used in this thesis are computed in a normalized action-angle coordinates; the change of variable (93) is first performed.

3.2.3 Long-range interactions

In the long-range model, the beams are offset by some distance D, which decreases to zero approaching the IP. However, the normalized distance $d = \frac{D(s)}{\sigma(s)}$ is constant near the interaction point (except very close to the IP) [25].

The physical distance D depends on the beam β's and on the crossing angle Θ_c.

$$D(s) \approx (\sqrt{\beta_x(s)\beta^*} + \sqrt{\beta_y(s)\beta^*})\frac{\Theta_c}{2} \tag{53}$$

where β^* is defined as the round beam β at the interaction point. Given the 1σ emmitance ϵ, the normalized crossing angle is defined as

$$\Theta_c^* = \Theta_c\sqrt{\frac{\beta^*}{\epsilon}}. \tag{54}$$

This allows for the normalized distance (d), used to for beam-beam analysis (66), to be written in terms of the normalized crossing angle (Θ^c)

$$d_{x,y} \approx [1 + \sqrt{\frac{\beta_{y,x}(s)}{\beta_{x,y}(s)}}]\frac{\Theta_c^*}{2}. \tag{55}$$

For the round beam, $\beta_x = \beta_y$. So, for $D = \sqrt{D_x^2 + D_y^2}$. (45) becomes

$$\Phi = \frac{ne}{4\pi\epsilon_0} \int_0^\infty \frac{e^{-\frac{(r+D)^2}{2\sigma^2+q}}}{(2\sigma^2+q)} dq. \tag{56}$$

This results in a constant (0^{th} order) force at the origin, causing closed orbit distortion.

The long-range model captures effects such as dependence of dynamic aperture and integrated loss on normalized separation. This has been studied in simulations and experimentally. Namely, it was experimentally observed in 2011 [30], that significant losses occur at IP1 for bunches when separation is around 5 σ for a 3.5 TeV beam with $\beta^* = 1.5$ m, $\Theta_c = 120$ μrad, $\epsilon = 2 - 2.5$ μm.

3.2.4 Long-range interactions and luminosity

Key parameters in long-range interactions are directly related to luminosity. Varying the separations of these long-range interactions requires changing the crossing angle, directly affecting the collision luminosity, which is defined as

$$L = \frac{f N_b N_1 N_2}{4\pi\sigma_x\sigma_y} \frac{1}{\sqrt{1+\phi^2}}. \tag{57}$$

N_1, N_2 denote the particle number per bunch, N_b is the number of colliding bunches (minimum 2). f denotes the revolution frequency, and σ_x, σ_y are the sigmas of the bunches describing their shape. $\frac{1}{\sqrt{1+\phi^2}}$ is the geometry factor, which depends on ϕ, the Piwinski angle. The Piwinski angle, which is linearly proportional to the crossing angle, describes relative orientation of the bunches during collision at the interaction points. For a horizontal crossing, where $D_y = 0$,

$$\phi = \frac{\theta_c \sigma_s}{2\sigma_x}. \tag{58}$$

For a vertical crossing, σ_y replaces σ_x. The interaction regions in the LHC use either horizontal or vertical crossing schemes.

3.2.5 Round beam vs elliptical beam

The elliptical beam model assumes elliptical Gaussian charge distribution for each bunch.

$$\rho = \frac{Ne^2}{\sigma_x \sigma_y (2\pi)^{3/2}} e^{-\frac{x^2}{2\sigma_x^2} - \frac{y^2}{2\sigma_y^2}}. \tag{59}$$

In analogy to previous cases, the potential is

$$\Phi = \frac{ne}{4\pi\epsilon_0} \int_0^\infty \frac{e^{-\frac{x^2}{2\sigma_x^2+q} - \frac{y^2}{2\sigma_y^2+q}}}{\sqrt{(2\sigma_x^2+q)(2\sigma_y^2+q)}} dq \tag{60}$$

where $\sigma_{x,y}$ denote Strong bunch sigmas.

For the proposed HL-LHC upgrade, a "flat" beam with β ratio of 1:4 is being considered. This translates to a factor of 2 difference in σ_x and σ_y in the regions from 30 to 50 meters away on both sides of the interaction point. The beam is always approximately round in the head-on region [25]. The breaking of cylindrical symmetry causes the problem to become inherently two dimensional.

The potential is then modified to account for long-range interactions:

$$\Phi = \frac{ne}{4\pi\epsilon_0} \int_0^\infty \frac{e^{-\frac{(x+D_x)^2}{2\sigma_x^2+q} - \frac{(y+D_y)^2}{2\sigma_y^2+q}}}{\sqrt{(2\sigma_x^2+q)(2\sigma_y^2+q)}} dq. \tag{61}$$

For this thesis, only round bunches will be considered. The round beam and elliptical beam potentials differ most from each other in the head-on regime. Fortunately, the bunch data show that bunches are highly round in the head-on regions. The only highly non-round bunches are in certain regions at a separation of 10-12.5 σ (see figure 5, table A). However, at this high separation, we are far outside of the beam's core; a simple Gauss's law argument show that the elliptical bunches can be replaced by round ones without much error. To reiterate, when separations are small, beams are approximately round. Beams are elliptical only in certain regions where the beam-beam separations are large enough to admit the approximation of elliptical beams with round ones. The round model was used for ease of computation. Elliptical bunches can be included in the model by using potential (61) at a computational cost.

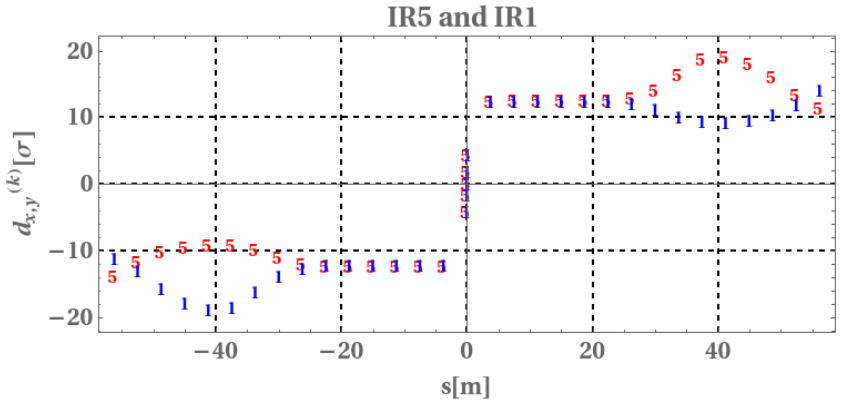

Figure 5: IR1 (labelled 1 in blue) IR5 bunches: (labelled 5 in red) normalized distances (in $[\sigma]$) as a function of distance from IP

3.3 Fourier analysis of beam-beam potential

The Fourier coefficients of the beam-beam potential in action-angle coordinates is used to compute an effective Hamiltonian for the system. Work done by [24] show that the beam-beam potential may be written using a modified 2D Bessel function. Following the derivation in [24]:

$$I_n(u,v) = \sum_{q=-\infty}^{\infty} I_{n-2q}(u) I_q(v) \tag{62}$$

where $I_n(x)$ are the well known modified Bessel functions of the second kind.

The generating functions for the modified 2D Bessel functions are

$$e^{-u_2 - u_1 \sin\phi_z + 2u_2 sin\phi_z} = \sum_{k=-\infty}^{\infty} i^k I_k(u_1, u_2) e^{ik\phi_z}. \tag{63}$$

In action-angle coordinates, let $\sigma^w_{x,y}$ denote Weak bunch sigma, and $\sigma_{x,y}$ denote Strong bunch sigma. Then the normalized amplitudes, given as numbers of sigmas, may be defined as $a_{x,y} = \frac{\sqrt{2A_{x,y}}}{\sigma_{x,y}}$(93). Using the Weak-Strong anti-symmetry [25], $\sigma^w_x = \sigma_y$, x and y may be written as

$$\begin{aligned} x &= \sigma_y a_x \sin\phi_x. \\ y &= \sigma_x a_y \sin\phi_y. \end{aligned} \tag{64}$$

This allows the writing of Weak bunch equations of motion in terms of variables normalized by the Strong bunch's σ's.

The 2D Weak-Strong long-range Hamiltonian may be written as

$$H = \int_0^1 \frac{dt}{tg(t)}(1 - e^{-t(Px+Py)}). \tag{65}$$

Where $P_{x,y} = \frac{1}{2}(\overline{d}_{x,y} + \overline{a}_{x,y}\sin\phi_{x,y})^2$, and are not momenta. The lowercase $d_{x,y}, a_{x,y}$ indicates that the separation $D_{x,y}$ and actions $A_{x,y}$ have been normalized by their respective $\sigma^w_{x,y}$. The bar coordinate $\overline{x}, \overline{y}$ simplifies the expression by removing factors of sigma ratios $r = \frac{\sigma_y}{\sigma_x}$ from the exponent. See appendix (D.3).

The Fourier coefficients are

$$c_{mn} = \int_0^1 \frac{dt}{tg(t)4\pi^2} \int_0^{2\pi}\int_0^{2\pi} e^{-im\phi_x} e^{-in\phi_y}(1 - e^{t(P_x+P_y)}) d\phi_x d\phi_y. \tag{66}$$

By performing the following substitution of variable,

$$\begin{aligned} u_{1(x,y)} &= t\overline{a}_{x,y}\overline{d}_{x,y} \\ u_{2(x,y)} &= -\frac{t}{4}\overline{a}^2_{x,y} \\ u_{3(x,y)} &= \frac{t}{2}\overline{d}^2_{x,y} \end{aligned} \tag{67}$$

the Fourier coefficients may be written as

$$c_{mn} = \int_0^1 \frac{dt}{tg(t)}[\delta^0_m\delta^0_n - i^{m+n} e^{u_{3(x)}+u_{3(y)}} e^{u_{2(y)}+u_{2(y)}} I_m(u_{1(x)}, u_{1(x)}) I_n(u_{1(y)}, u_{1(y)})]. \tag{68}$$

The 2D Bessel functions show a recursive relation; it is possible that the Fourier coefficients show similar behaviour [24].

3.4 Multiple interaction points

The LHC has 8 interaction regions, four of which hosts the experiments ATLAS, ALICE, CMS, and LHCb, where beams cross and collide. See figure 3.

The operational bunch spacing of 25 ns corresponds to 7.5 m. The collision separations are therefore 12.5 ns. A Weak bunch will have around 16 long-range encounters over a region of 120 m.

In coordinates normalized by emmittance, the beam-beam separation is constant over certain regions, and these encounters may be grouped into a single beam-beam interaction to simplify the model; this is used in parts of section 6.

Writing a Hamiltonian for the simple harmonic motion coupled to numerous beam-beam interaction located at different places around the LHC ring sounds like an impossible task. The "Lie operator" formalism, to be introduced in the next section, allows this to be done. [5]

3.5 Other known beam-beam effects

One of the important beam-beam effects not covered by beam-beam analysis in this thesis is the Pacman effect.

Pacman bunches differ from standard bunches in that they circulate past gaps near some IR instead of opposing bunches. This is due to the specific bunch spacing of the LHC described in [31]. These bunches suffer from slightly different tune shifts and orbit distortions caused by experiencing some gaps in place of some beam-beam impulses when compared to regular bunches. Since the machine is optimized for standard bunches, it is possible for Pacman bunches to suffer greater losses, leading to the eventual creation of more gaps and additional Pacman bunches [32]. The details of the Pacman effect in the LHC may be found in [31][33].

Coherent modes mentioned in 3.2.1 occur when opposing beams oscillate in phase (σ mode) or π out of phase π-mode. These effects are not seen in a Weak-Strong model. These effects of these have been studied experimentally [27] and predicted analytically [28].

Effects which couple momentum deviations such as tune chromaticity are not covered by the beam-beam model in this thesis. The tune chromaticity ν' measures the dependence of the tune on the momentum deviation $\nu = \nu_0 + \nu' \frac{\Delta p}{p}$. The tune chromaticity for a linear ring is on the order of the ring's tune, and must be corrected for. The LHC's ν' is corrected to a value around 15. There are studies on the effects of chromaticity, and momentum spread, in the context of LHC beam-beam using numerical simulations [7]. With the Lie algebra method used by this thesis, momentum deviations can be coupled into the system by extending the phase space [14].

[5] An effective Hamiltonian is computed, valid in the regime of small beam-beam potential

4 Lie Algebraic approach

This section will present the mathematical background. It will introduce the Poisson bracket Lie algebra, and some equivalent Lie algebras, from which formulae and results in this thesis are derived. It will also present the "Lie algebra formalism" used in non-linear accelerator physics. This formalism, invented by Alex.J.Dragt [3], popularized by Alex Chao [14], writes Lie derivatives and exponential maps in a way that naturally extends matrix formalism notations. In this notation,

$: H :$ denotes a "Lie operator,"

$e^{-:H:\tau}$ is its exponential map and denotes a "Lie Map.", and τ is the independent variable

This will be elaborated on in the following sections.

4.1 Introduction to Lie groups and Lie algebras

Lie groups and Lie algebras are abstract mathematical objects with many uses in physics. They are seen in physics as differentiable, parameter dependent transformations. Some examples, time evolution with time as a parameter, spatial translations with distances as parameters. Transformations in classical mechanics, operators in quantum mechanics, and symmetry groups are all Lie groups (or at least can be described in the language of Lie groups). In this picture, the Lie algebra associated to a Lie group is the infinitesimal transformation associated to the Lie group's continuous transformation. A Lie algebra can be used to generate its Lie group via the exponential map (given some topological assumptions).

These Lie groups often have simple matrix representation. This is always true when the action of the Lie group is restricted to a vector space of column vectors. In this case, the Lie algebra also corresponds to an algebra of matrices. For example, the Lie group SO_3 acting on 3 dimensional column vectors can be represented by the well known 3 dimensional rotation matrices. The corresponding Lie algebra is three dimensional; its basis can be found by Taylor expanding the general (3 arbitrary angles) SO_3 rotation matrix along each of the rotation angles. Unfortunately, for the purpose of studying beam-beam and more generally Hamiltonian mechanics using a Lie algebra formalism, a matrix representation is in general not possible.

4.2 Definition and representations of Lie groups and Lie algebras

Mathematically, a Lie group is defined as a group with smooth group operations. They can also be viewed as smooth manifolds, in which case the Lie algebra corresponds the tangent space at the Identity. In this picture, a Lie groups and Lie algebras can be represented geometrically.

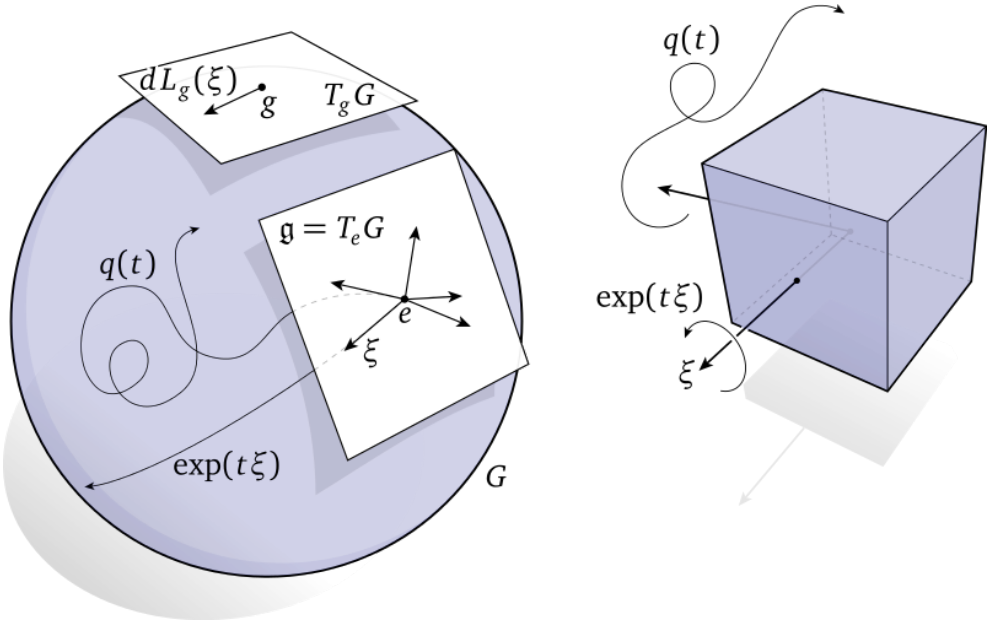

Figure 6: Left: A diagrammatic representation of a fictitious Lie group as a manifold Right: The action of two of its one-parameter subgroups on a box (right) [34]

Figure 6 is diagrammatic representation of a fictitious Lie group and its action. It is not a representation of an actual Lie group.

The set of smooth and invertible maps from a space to itself is a Lie group (diffeomorphism group). Its Lie algebra is the set of vector fields on the space. In this sense, if some subset of maps preserves the system, or certain aspects of the system, we say that it is a symmetry. So, Lie groups often describe symmetries. Indeed, the set of canonical transformations on a phase space is one such example. It is called the symplectomorphism group.

Lie algebras are the first order "approximations" of Lie groups. When Lie groups are viewed as manifolds, the Lie algebra is the tangent space at identity. When viewed as maps, Lie algebras can either be represented as vector fields (on the base space

which is acted on by the Lie group), first order differential operators, matrices, etc, all of which give a local representation of a map, and are equivalent. If the Lie group in question is a symmetry group, its Lie algebra "generates" the symmetry.

The set of canonical transformations on a phase space is called a Lie group called the symplectomorphism group. It is the set of phase space maps which preserves equations of motions and a set of invariants called Poincare integrals invariant [35].

4.3 Symplectic transformations as a Lie group

As mentioned in the previous section: given a phase space, the set of all maps is called the diffeomorphism group of the phase space. It is known that the Lie algebra of a diffeomorphism group on a manifold is the set of vector fields on the manifold [36]. Vector fields in this context are defined by using differential operators (via $\frac{\partial}{\partial x} \to \hat{x}$).

The set of symplectomorphisms is a Lie subgroup of the diffeomorphism group; its Lie algebra is the set of all symplectic vector fields.

This symplectic condition may also be viewed as a condition on the Jacobian matrices of symplectic maps; the Jacobian matrix must belong to the Symplectic Matrix group of appropriate dimension.

The exponential map generates a Lie group element from Lie algebra elements.

4.3.1 The geometry of phase space

In the symplectic geometry formulation of classical mechanics, the phase space is a manifold with a non-degenerate canonical 2-form $dp \wedge dq$, usually denoted ω in coordinate free notation. This can be interpreted as the oriented differential area of the parallelogram created by two infinitesimal vectors $dp\hat{p}$ and $dq\hat{q}$.

The set of canonical transformations, called symplectomorphisms, are the set of maps which preserves this canonical two form. Time evolution is one such transformation. These maps have Jacobian matrices with unit determinant and preserve equations of motion. These form a Lie group, and are therefore also a manifold. Its Lie algebra corresponds to the set of symplectic vector fields on the phase space. (4.4.1)

The canonical 2-form can be used to define a symplectic gradient $(-\frac{\partial}{\partial p}, \frac{\partial}{\partial q})$, which generates symplectic vector field from Hamiltonians. The "time evolution" of these Hamiltonians are canonical transformations.

4.4 Poisson bracket Lie algebra of Phase Space Functions

A Phase Space Function in the context of this thesis is defined to be a function from the phase space to the real number line. Examples are Hamiltonians, phase space density functions, scalar potentials. This set of function form a Lie algebra with the Poisson bracket as Lie bracket.

Hamilton's equations 2 can be written in terms of the Poisson bracket;

$$\begin{aligned} \frac{dq}{dt} &= -\{H, q\} = -\frac{\partial H}{\partial q}\frac{\partial q}{\partial p} + \frac{\partial H}{\partial p}\frac{\partial q}{\partial q} = \frac{\partial H}{\partial p}. \\ \frac{dp}{dt} &= -\{H, p\} = -\frac{\partial H}{\partial q}\frac{\partial p}{\partial p} + \frac{\partial H}{\partial p}\frac{\partial p}{\partial q} = -\frac{\partial H}{\partial q}. \end{aligned} \tag{69}$$

In Lie operator notation [3], this becomes

$$\begin{aligned} \frac{dq}{dt} &= - : H : q \\ \frac{dp}{dt} &= - : H : p. \end{aligned} \tag{70}$$

In this notation, given H, we define a linear operator $: H :$ acting on functions $f(q, p)$ as

$$: H : f = \{H, f\}. \tag{71}$$

.

$: H :$ is called the Lie operator of H, and corresponds to a Lie derivative along the Hamiltonian vector field X_H, generated by H. In the language of group theory, $: H :$ is also called a generator; it generates the one-parameter diffeomorphism group $e^{-:H:\tau}$. This is often written as $e^{:f_H:}$, where $: f_H := - : H : \tau$ is the generator of the map. For one-turn type maps, $\tau = 1$. For the purpose of accelerator physics, each magnet has its own Hamiltonian. It is in theory possible to construct a piece-wise continuous Hamiltonian for the whole system of sequential magnets and drifts. In practice, maps are constructed to propagate the beam through each magnet. The linear betatron motion one-turn map for the whole ring is however simple to write down. Using the Courant-Snyder parameters of the accelerator ring, a one-turn map

may be constructed which treats the ring as a black box.

To solve (70), we recall the matrix D.E equation, for constant matrix A.

$$\frac{d\vec{x}}{dt} = A\vec{x}. \tag{72}$$

is given by the matrix exponential

$$\vec{x}(t) = e^{At}\vec{x}(0). \tag{73}$$

If A is not constant, then it may not commute with itself at different times, in which case the solution must be calculated via some infinite series.

Just as a matrix is a linear operator in a finite dimensional vector space of column vectors, $:H:$ is an linear operator in an infinite dimensional vector space of functions. The solutions to (70) are given by the exponential map (H is assumed to be time independent):

$$\begin{bmatrix} q(t) \\ p(t) \end{bmatrix} = e^{-:H:t} \begin{bmatrix} q_0 \\ p_0 \end{bmatrix}. \tag{74}$$

We note that despite the Lie algebra of phase space functions being infinite dimensional, bases may be constructed. For example, it can be shown in appendix (der. D.1) that the eigenbasis of the simple harmonic oscillator generator $1/2 : p^2 + q^2 :$ are the action-angle circular harmonics $e^{in\phi}$. Furthermore, any quadratic Hamiltonian $H = aP^2 + bPQ + cQ^2$ can be transformed into $1/2(p^2 + q^2)$ via a rotation and a re-scaling. So, the natural basis of the quadratic Hamiltonian is the set of circular (Fourier) harmonics. This will be used later on to compute the effective Hamiltonian.

4.4.1 Lie operators as symplectic vector fields

In the spirit of geometry, the Lie operator Lie algebra with commutator bracket can also be identified with the symplectic vector field Lie algebra with commutator (vector field Lie derivative) Lie bracket. Using the differential operators/vectors equivalence seen in differential geometry [36], these two Lie algebras can be viewed as the algebraic and geometric representation of the same object.

Consider

$$:h: := \frac{\partial h}{\partial q}\frac{\partial}{\partial p} - \frac{\partial h}{\partial p}\frac{\partial}{\partial q}. \tag{75}$$

By identifying $\frac{\partial}{\partial p}$ to $\hat{p}$ and $\frac{\partial}{\partial q}$ to $\hat{q}$, each Lie operator $: h :$ can be identified to a vector field. $X_h = \frac{\partial h}{\partial q}\hat{p} - \frac{\partial h}{\partial p}\hat{q} = (-\frac{\partial h}{\partial p}, \frac{\partial h}{\partial q})$.

Furthermore, the Lie brackets correspond as follows (Appendix.D.2):

$$[: h :, : g :] =: \{h, g\} : \ \rightarrow X_{\{h,g\}} \tag{76}$$

using (141) and the definition of X_f, $X_{\{h,g\}} = X_h X_g - X_g X_h$. This corresponds to the definition of Lie derivative of the vector field X_g along the vector field X_h.

For the simple Harmonic oscillator $H = x^2 + p^2$, the symplectic vector fields are $X_h = S\boldsymbol{\nabla} H$, where $S = \begin{bmatrix} 0 & 1 \\ -1 & 0 \end{bmatrix}$, and $\boldsymbol{\nabla}$ denotes the phase space gradient $(\frac{\partial}{\partial x}, \frac{\partial}{\partial p})$.

Figure 7 plots X_h in phase space. It should be clear that the integral curves of this vector field trace out circles which are phase space trajectories of the given Hamiltonian. The curves are traced counter-clockwise because the phase space is defined as (93), with the angle coordinate starting on the positive x-axis and going counter clockwise.

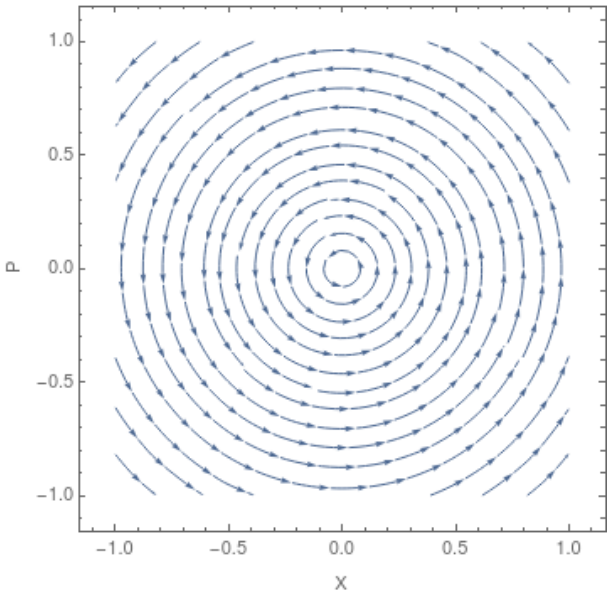

Figure 7: Symplectic Vector Field of a simple harmonic oscillator in 2D phase space

4.4.2 Time (or s) evolution as the exponential map of this Lie algebra

The exponential map can be used to solve (70). In particular for quadratic Hamiltonian, the exponential map reduces to a matrix exponential.

As a worked example, consider the relativistic electromagnetic Hamiltonian (6). Taking the potential to be that of a quadrupole, and expanding the Hamiltonian to second order in the low transverse energy limit:

$$H_s = K(x^2 - y^2) + P_x^2 + P_y^2. \tag{77}$$

The equations of motions are

$$\begin{aligned} x' &= -:H:x \;=\; \frac{\partial H}{\partial P_x} = \;P_x, \\ y' &= -:H:y \;=\; \frac{\partial H}{\partial P_y} = \;P_y, \\ P_x{}' &= -:H:x \;=\; -\frac{\partial H}{\partial x} = \;-Kx, \\ P_x' &= -:H:x \;=\; -\frac{\partial H}{\partial y} = \;Ky. \end{aligned} \tag{78}$$

In phase space coordinates, the action of $:H:$ can be written as a matrix DE:

$$\frac{d}{ds}\begin{bmatrix} x \\ P_x \\ y \\ P_y \end{bmatrix} = \begin{bmatrix} 0 & 1 & 0 & 0 \\ -K & 0 & 0 & 0 \\ 0 & 0 & 0 & 1 \\ 0 & 0 & K & 0 \end{bmatrix}\begin{bmatrix} x \\ P_x \\ y \\ P_y \end{bmatrix}. \tag{79}$$

Let $\vec{z} = (x, P_x, y, P_y)$, writing the matrix differential equation as $\vec{z}' = A\vec{z}$, the solutions $\vec{z}(s) = e^{As}\vec{z}(0)$ are written in terms of the matrix exponential:

$$e^{As} = \sum_{k=0}^{\infty} \frac{A^k}{k!} = I + (As) + \frac{1}{2}(As)^2 + O(s^3). \tag{80}$$

It is simple to verify by grouping even and odd powers of A that the power series

converges to :

$$e^{As} = \begin{bmatrix} \cos\left(\sqrt{|K|}s\right) & \frac{\sin\left(\sqrt{|K|}s\right)}{\sqrt{|K|}} & 0 & 0 \\ -\sqrt{|K|}\sin\left(\sqrt{|K|}s\right) & \cos\left(\sqrt{K}s\right) & 0 & 0 \\ 0 & 0 & \cosh\left(\sqrt{|K|}s\right) & \frac{\sinh\left(\sqrt{|K|}s\right)}{\sqrt{|K|}} \\ 0 & 0 & \sqrt{|K|}\sinh\left(\sqrt{|K|}s\right) & \cosh\left(\sqrt{K}s\right) \end{bmatrix} \tag{81}$$

which matches the known solutions.

It is important to note that a nth-order Hamiltonian Lie operator : H_n : will map a mth order polynomial P_m to a polynomial of order $(m + n - 2)$. Therefore, only a quadratic Hamiltonian Lie operator : H_2 :, representing linear systems, can map a polynomial to a polynomial of same order. Therefore, only : H_2 : has square matrix representation in linear or polynomial vector spaces. The matrix representation can easily be exponentiated.

In general, $e^{-:H:\tau}$ must be evaluated as a truncated power series. The evaluation consists of computing nested Poisson brackets. Fortunately, the truncation is symplectic at every order.

For accelerator physics, the exponential maps for various thin elements are simple to write down; see appendix (C). Truncation order can be chosen for arbitrary precision, and the guaranteed symplecticity makes this formalism natural for treating non-linear elements. However, due to the non-commutativity of Lie operators, the product of maps is not straight forward. Nonetheless, it must be computed to obtain the total map of a series of elements.

4.5 Product of exponential maps of non-commuting operators

The product of exponential maps of non-commuting operators are not straight forward to compute. It must in general be expressed using the adjoint representation (appendix E), or represented as nested Lie brackets. Let X, Y be members of a Lie algebra g. Consider

$$e^X e^Y = e^Z. \tag{82}$$

$Z = X + Y$ if and only if $[X, Y] = 0$. In other cases, one of the Baker-Campbell-Hausdorff (BCH) formulae must be used.

The closed form BCH formula can be derived using the derivative of the exponential map, assuming convergence.

The most well known BCH formula is an expansion in powers of X, Y, and nested commutators. This version is to be used when X and Y are of similar "size". I.e. formula (83) is perturbative in both operator X and Y, which are assumed to be close to identity.

$$Log(e^X e^Y) = X + Y + \frac{1}{2}[X,Y] + \frac{1}{12}([X,[X,Y]] - [Y,[X,Y]]) + ... \tag{83}$$

A second version is a linear expansion in Y. Y is assumed to be close to the identity; no such assumption is made on X. The formula contains dependence on X in closed form, albeit as an expression in its adjoint representation. This is the version used in this thesis for computing of the effective Hamiltonian for beam-beam.

$$Log(e^X e^Y) = X + \frac{ad_x}{1 - e^{-ad_x}} Y + O(Y^2). \tag{84}$$

Assuming convergence of the product, the closed form version can be written [37]

$$Log(e^X e^Y) = X + \int_0^1 \frac{d(e^{adX} e^{tadY})}{dt} Y dt. \tag{85}$$

From this, the two previous versions (83,84) can be easily derived.

4.6 Lie operator formalism

A function of phase space variable $H(q,p)$ can associated to a Lie operator $:H:$. The action of $:H:$ is defined via its Poisson bracket.

$$:H:G = \{H,G\} \tag{86}$$

The Lie operator maps a scalar function to a scalar function and a vector field to a vector field. I.e.

$$:H: \begin{bmatrix} X(t) \\ P(t) \end{bmatrix} = \begin{bmatrix} :H:X(t) \\ :H:P(t) \end{bmatrix}. \tag{87}$$

The Lie operator $:H:$ is linear in H. That is to say $:aH_a + bH_b:=: a:H_a: + b:H_b:$.

Using the exponential map, a Lie map $e^{-:H:\tau}$ can be created. This map propagates

the system with Hamiltonian H forward by τ.

In an accelerator, the Lie of consecutive elements with Hamiltonian H_1, H_2 can be written as the product of their Lie maps $e^{-:H_1:L_1}e^{-:H_2:L_2}$. The independent variable is also switched from t to s. When s is the independent variable, the canonical momentum P is often called x', and is unitless. Note the ordering of the product is the reverse of matrix maps.

The similarity transformation of Lie maps is identical to that of matrices.

$$e^{:f:}e^{:g:}e^{-:f:} = e^{:e^{:f:}g:}. \tag{88}$$

The exponential map of a function of phase space variable is the function acting on the exponential mapped variables

$$e^{:f:}g(q,p) = g(e^{:f:}q, e^{:f:}p). \tag{89}$$

4.7 Unperturbed Hamiltonian

The quasi-harmonic transverse (betatron) motion of a particle in an accelerator, when viewed turn by turn at some fixed location, can be represented by the Courant-Snyder Hamiltonian which generates a one-turn map. The μ's, γ's, and α's are functions of the independent variable s. Using $F = -H$,

$$F_2 = -\frac{\mu_x}{2}(\gamma_x x^2 + 2\alpha_x x x' + \beta_x x'^2) - \frac{\mu_y}{2}(\gamma_y y^2 + 2\alpha_y y y' + \beta_y y'^2) \tag{90}$$

where $x' = \frac{dx}{ds}$, and $y' = \frac{dy}{ds}$ are the canonical momenta. This is the equation of a Courant-Snyder ellipse in phase space multiplied by tunes. By treating it as the Hamiltonian of a one-turn map, its solution curves exactly traces Courant-Snyder ellipses. By introducing the following change of coordinate, the ellipse is mapped

onto a circle.

$$\begin{aligned} x' &\to \frac{-\alpha_x x + P_x}{\sqrt{\beta_x}} \\ x &\to \sqrt{\beta_x} X \\ y' &\to \frac{-\alpha_y y + P_y}{\sqrt{\beta_y}} \\ y &\to \sqrt{\beta_y} Y. \end{aligned} \tag{91}$$

The resulting Hamiltonian is a simple harmonic oscillator:

$$F_2 = -\frac{\mu_x}{2}(X^2 + P_x^2) - \frac{\mu_y}{2}(Y^2 + P_y^2). \tag{92}$$

It is simple to verify that this generates rotations in $X - P_x$, $Y - P_y$ via $e^{:F_2:\theta}$, where θ indexes turn angle or turn number. Furthermore, in this coordinate, both X and P_x have units of $[L]^{\frac{1}{2}}$.

The following change of coordinate brings F_2 to action-angle form:

$$\begin{aligned} X &\to \sqrt{2A_x}\sin\phi_x \\ Y &\to \sqrt{2A_y}\sin\phi_y \\ P_x &\to \sqrt{2A_x}\cos\phi_x \\ P_y &\to \sqrt{2A_x}\cos\phi_x. \end{aligned} \tag{93}$$

We note that some authors denote this action with dimensions $[A_{x,y}] = [L]$ as $J_{x,y}$. and reserve $A_{x,y}$ for $J_{x,y}\beta_{x,y}$. We use Chao [14]'s notation. The resulting Hamiltonian is

$$-H = F_2 = -\mu_x A_x - \mu_y A_y. \tag{94}$$

It is simple to check that the circular harmonics are eigenfunctions of $:F_2:$. See appendix D.1.

$$:F_2: e^{im\mu_x\phi_x} e^{in\mu_y\phi_y} = i(m\mu_x + n\mu_y) e^{im\mu_x\phi_x} e^{in\mu_y\phi_y}. \tag{95}$$

4.8 Perturbation on the oscillator

Suppose there is a perturbation to the simple harmonic motion, generated by F_p. In the Lie formalism, this can be written as the product of Lie maps.

$$e^{:F_{eff}:} = e^{:F_2:} e^{:F_p:} \tag{96}$$

Since the F_p is treated as a perturbation, it makes sense to use (84) to compute the effective Hamiltonian, where the adjoint representation is taken in the Poisson bracket:

$$\begin{aligned} :F_{eff}: &=: F_2 : + : \frac{:F_2:}{1-e^{-:F_2:}} F_p : \\ F_{eff} &= F_2 + \frac{:F_2:}{1-e^{-:F_2:}} F_p. \end{aligned} \tag{97}$$

$\frac{:F_2:}{1-e^{-:F_2:}}$ should be understood as an operator power series acting on F_p.

$$\frac{:F_2:}{1-e^{-:F_2:}} = I + \frac{:F_2:}{2} + \frac{:F_2:^2}{12} - \frac{:F_2:^4}{720} + O(:F_2:^6). \tag{98}$$

However, away from resonance, the denominator is non-zero. The power series therefore converges to the analytic function. I.e. wherever the spectrum of $\frac{:F_2:}{1-e^{-:F_2:}}$ is bounded, its power series converges; it can then be understood as an analytic function. In this case the eigenvalue property of analytic functions can be used [6] to evaluate the expression. If F_p can be written in the eigenbasis of $:F_2:$ as $\sum_k c_k F_k$, the expression (97) can be written as

$$F_{eff} = F_2 + \sum_k \frac{\lambda_k}{1-e^{-\lambda_k}} c_k F_k. \tag{99}$$

When F_2 is a simple harmonic oscillator, the eigenfunctions are the circular harmonics. Therefore, the eigenbasis decomposition is a Fourier decomposition. (Appendix D.1) One should note that for an impulse, $:F_p := -:H_p:$; these Fourier coefficients are negatives of ones computed from the impulse Hamiltonian (68).

$$F_{eff} = F_2 + \sum_{m,n} \frac{i(m\mu_x + n\mu_y)}{1-e^{-i(m\mu_x+n\mu_y)}} c_{mn} e^{im\mu_x\phi_x} e^{in\mu_y\phi_y}. \tag{100}$$

[6] Given an linear operator M, $F(M)\vec{x} = F(\lambda)\vec{x}$ if $M\vec{x} = \lambda\vec{x}$ is the eigenvalue equation.

4.8.1 Multiple impulses

For the beam-beam impulse, the Fourier decomposition is given in section (3.3). For multiple impulse like perturbations, an effective map can be computed. Let F_j denote the jth impulse, then

$$\begin{aligned} e^{:F_{total}:} &= \prod_j e^{:F_j:} \\ &= e^{\sum_j :F_j: + \sum_{i \neq j} \frac{1}{2}[:F_i:,:F_j:] + \ldots}. \end{aligned} \tag{101}$$

The $[: F_i :, : F_j :]$ terms come from (83), and must be computed in an analysis to "beam-beam strength" squared. Furthermore, a second order version of (84) must be used. However, when considering only an analysis linear in beam-beam Hamiltonian, the commutator of two beam-beam impulse can be dropped.

The contribution to beam-beam of all interaction regions can then be summed

$$\begin{aligned} e^{:F_{total}:} &= e^{:\sum_j F_j:} \\ : F_{total} : &=: \sum_j F_j : . \end{aligned} \tag{102}$$

Substituting (102) into (97), and performing the same procedure as (100), with the "$^{(j)}$" superscript labelling different beam-beam impulses. The Fourier coefficients $c_{mn}^{(j)}$ are the negatives of (68) since $F_{bb} = -H_{bb}$.

$$F_{eff} = F_2 + \sum_j \sum_{n,m=-\infty}^{\infty} \frac{i(m\mu_x + n\mu_y)}{1 - e^{-i(m\mu_x + n\mu_y)}} c_{mn}^{(j)} e^{im(\mu_x + \phi_x)} e^{in(\mu_y + \phi_y)}. \tag{103}$$

This expression implicitly assumes that the impulses are located at the same phase. This is not the case in reality. A similarity transformation can be used to introduce the varying phase at different impulse location.

$$e^{:F(\psi_x, \psi_y):} = e^{-:f_2:} e^{:F(0):} e^{:f_2:}. \tag{104}$$

where $e^{:f_2:}$ is the appropriate rotation matrix in phase space such that f_2 generate a rotation by $-\psi_x$ in the $X - P_x$ plane, and $-\psi_y$ in the $Y - P_y$ plane. Then using the

similarity transformation rule of Lie operators, the transformation can be written as

$$e^{:F(\psi_x,\psi_y):} = e^{:(e^{:f_{2rot}:}F(0)):}. \tag{105}$$

The action of a rotation matrix [7] in polar coordinates is a simple translation in angle. So after shifting all the F_j' s, each located at a shifted phase of $(\Delta\mu_x^{(j)}, \Delta\mu_y^{(j)})$ to their appropriate phase,

$$F_{eff} = F_2 + \sum_j \sum_{n,m=-\infty}^{\infty} \frac{i(m\mu_x + n\mu_y)}{1 - e^{-i(m\mu_x+n\mu_y)}} c_{mn}^{(j)} e^{im(\mu_x+\phi_x+\Delta\mu_x^{(j)})} e^{in(\mu_y+\phi_y+\Delta\mu_y^{(j)})}. \tag{106}$$

Multiplying and dividing each summation term by $e^{\frac{i}{2}(m\mu_x+n\mu_y)}$, substituting in $F_2 = -\mu_x A_x - \mu_y A_y$, this can be written as:

$$F_{eff} = -\mu_x A_x - \mu_y A_y + \sum_j \sum_{n,m=-\infty}^{\infty} \frac{(m\mu_x + n\mu_y)}{2\sin\left(m\frac{\mu_x}{2} + n\frac{\mu_y}{2}\right)} c_{mn}^{(j)} e^{im(\frac{\mu_x}{2}+\phi_x+\Delta\mu_x^{(j)})} e^{in(\frac{\mu_y}{2}+\phi_y+\Delta\mu_y^{(j)})}. \tag{107}$$

This is the effective Hamiltonian $H_{eff} = -F_{eff}$ of the combined system; it is used to study the frequency space in the following section.

[7] The angle in phase space has been defined to go clockwise, therefore the rotation matrix rotates in the opposite direction as expected

5 Implementation

5.1 The effective Hamiltonian for multiple interaction points

In this effective Hamiltonian approach, each bunch in the Strong beam in the interaction region is treated as the source of a beam-beam impulse to the weak beam. Bunches in the same beam can sometimes be grouped together for computational purpose. This type of grouping normally requires the use of BCH formulae (83) (84). However, for two bunches with the same phase and separation, their Lie operators are identical. Higher order BCH terms are identically zero; the product of their Lie maps may be written as

$$\prod_{j=1}^{N} e^{:F_{bunch}:} = e^{N:F_{bunch}:}. \tag{108}$$

The preliminary beam-beam model is a Lie map of two interaction regions. Each IR consists of 9 long-range interactions at a normalized separation (55) of 12.5 σ, followed by a head-on interaction phase shifted by $\approx \pi/2$, which is followed by another 9 long-range interactions phase shifted by $\approx \pi/2$ with respect the head-on interaction. See figure 5.

The interactions regions are also phase shifted from each other. For the nominal LHC, the phase shifts between IR1(ATLAS) and IR5(CMS) is $\approx 64.2\pi$ in μ_x and $\approx 60.7\pi$ in μ_y. These values are used for the model.

These interactions are all combined into one Lie map using the lowest order BCH formula. The effective Hamiltonian, of the form (107), can be read off from the Lie operator which generates the map.

The computing was done in Mathematica 11. The main challenge was in the calculation of a large number of Fourier coefficients. The two main approaches were numerical integration, and evaluation of generalized 2D Bessel functions of the second kind.

A more detailed model, built from the bunch data, treating each Strong beam bunch as a separate impulse each with their own normalized separations and phase shifts was also implemented using the same Mathematica code. Specifically, sections 6.1, 6.3, 6.4, 6.5 use the detailed model. Sections 6.2.1, and 6.2.2 use the preliminary idealized model.

5.2 Numerical computation of Fourier coefficients

The numerical computation of Fourier coefficients is done using the two dimensional modified Bessel-I functions of section (3.3). The evaluation of the two dimensional modified Bessel-I functions is implemented in two ways; via its definition in section (3.3) and via the numerical integration of its generating function,

$$I_n(u,v) = \frac{1}{2\pi}\int_0^{2\pi} e^{u\cos\theta + v\cos 2\theta - in\theta} d\theta. \tag{109}$$

5.3 "Tune-scan" using Hamiltonian

Tune-scans in the context of accelerator physics usually means a frequency space map of a quantifier of stability. These maps are performed to identify potential working point(s), the chosen bare tune at which the accelerator operates. Some important quantifier of stability of the accelerator at a given tune, such as the dynamic aperture, is computed in frequency space using the numerical simulation of a large number of particles. This is shown as a frequency domain plot.

The dynamic aperture drops at dangerous resonances. Previous work for 1D tune-scans show that these drops correspond to frequencies at which the effective Hamiltonian becomes singular [38].

In this thesis, "Tune-scan using invariant" refers to plotting the invariant (effective Hamiltonian) in frequency space. The invariant experiences singularities at resonance lines (section 5.3.1). With the assumption that more dangerous resonance lines cause stronger singularities in the invariant and occupy a wider area in tune space, these plots perform the same function as a traditional tune-scan at a much lower computational cost. They are however limited by their inability to give an explicit dynamic aperture value. If a tune-scan is desired, these plots can act as preliminary tools for selecting specific regions on which to perform a scan, thus reducing computational cost.

5.3.1 Resonance lines in tune space

Let m, n, q be integers. The set of linear equations $m\mu_x + n\mu_y = 2\pi q$, or equivalently $m\nu_x + n\nu_y = q$ densely populate the 2D space of tunes. See figure 8. The plots are given with tunes ν_x, ν_y, as "per-turn frequencies" such that the axes are labeled without factors of 2π. The formulae will use angular frequencies μ_x, μ_y, in radians to

absorb factors of 2π. The region of interest was chosen to show nearby resonances of the operating frequency of the HL-LHC (64.31,60.32). The tune plot in ν is periodic in a 2D integer lattice, therefore the region near $(0.31, 0.32)$ is plotted instead.

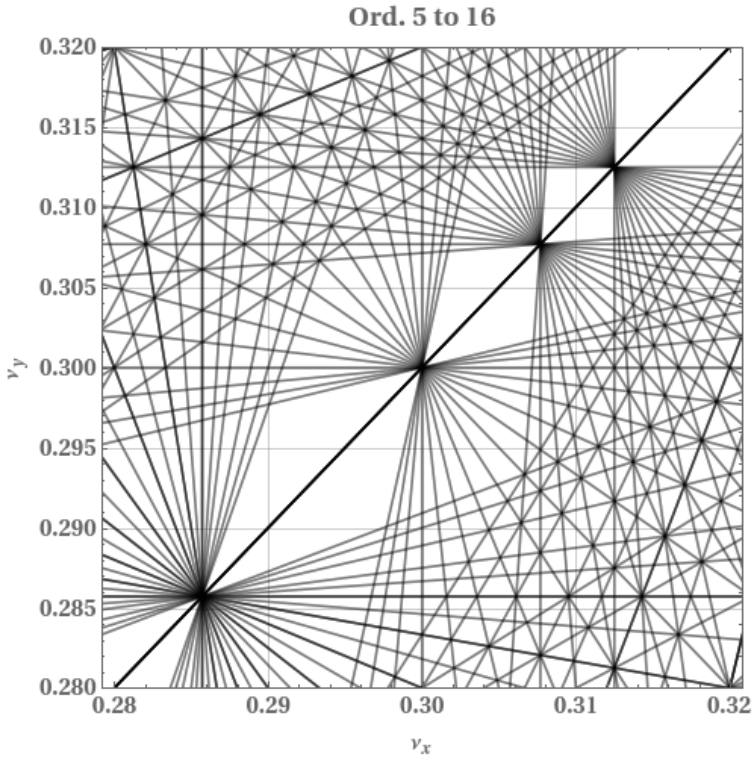

Figure 8: Resonance lines: Order 5 to 16

The main diagonal is defined as the equation $\nu_x - \nu_y = 0$. The resonances of the same order q intersect along the main diagonal. These are, as they appear up the main diagonal of this plot, $q = 14, q = 10, q = 13, q = 16$.

5.3.2 Beam-beam tune footprint

As stated in section (2.6.1), the amplitude dependence of the tune shift causes an ensemble of particle to form a distribution in frequency space. The tune footprint is the 2 dimensional plot of detuning at machine bare tune caused by this amplitude dependent tune spread.

From Hamilton's equations, the tune is given by

$$\frac{d\phi_{x,y}}{dk} = \frac{\partial H}{\partial A_{x,y}}. \tag{110}$$

For a distribution of particle with different amplitudes, the tune shift will also be a distribution in tune space. Away from resonance, we can bring the effective Hamiltonian to Normal form (Section 9.8 in [14]), $H_eff = -f_2 + C_0(A_x, A_y)$, where $C_0(A_x, A_y)$ is the 0th order Fourier coefficient of the beam-beam Hamiltonian. In this form, the beam-beam tune spread is

$$\Delta\mu_{x,y} = \frac{\partial C_0}{\partial A_{x,y}}. \tag{111}$$

The footprint can be plotted by analytically using this C_0 derivative, or by Tracking via Fast Fourier Transforms [24]. Although this thesis does not study tune footprints, their existence should be acknowledged when studying the tune space and resonances. It is important to choose a working point such that the footprint does not partially land near dangerous resonances. Figure 9 shows the shape of the beam-beam footprint.

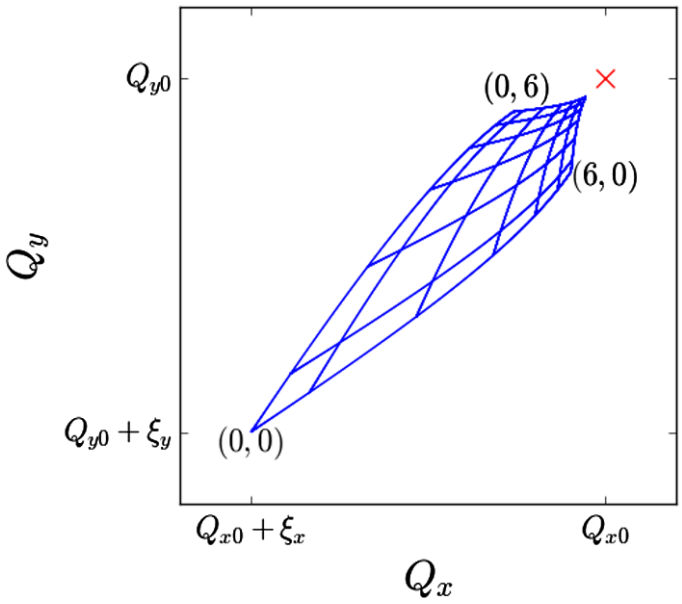

Figure 9: Figure 2 in [7], a beam-beam tune footprint for $0 \leq (x, y) \leq 6\sigma$. Red x denotes the working point. $Q_x = \nu_x, Q_y = \nu_y$.

The beam-beam parameter ξ (50) denotes the tune shift experienced by a zero amplitude particle during head-on interactions. In figure 9, ξ_x, ξ_y are used to differentiate the zero amplitude vertical and horizontal tune-shifts for a head-on interaction when the Strong bunches are not round.

5.3.3 Resonance width

Betatron resonances are not analogous to the resonances found in electric circuits. The resonance lines exhibit a lock-on width, which defines a region surrounding each resonance line. In this region, a particle's tunes experience oscillations due to perturbations, with amplitudes comparable to the region's width. These oscillations are caused by the perturbation(s) driving the resonance. The particle's oscillating tunes will eventually hit the resonance. Once at a resonance of some order, say n, the particle repeat its motion every n turn while accumulating periodic impulses. This may result in amplitude growth and loss of the particle (Wilson in [9]). Collins [39] uses beam loss as a criterion for width, whereas Chao [14] uses an intrinsic definition. This thesis will follow Chao's definition of resonance width as amplitude of the tune oscillation near resonance.

The frequency space is densely populated by resonance lines, some of which have unstable neighbourhoods. Namely, the resonance lines with positive slopes are "difference resonances" which are stable due to constraints imposed on the actions. To contrast, the resonance lines with negative slopes are "sum resonances" which are unstable. This is because $nA_x - mA_y$ is a constant of motion, which constrains the maximum values of A_x and A_y when m and n are of opposite sign; no such constraint exist when they share the same sign.

The resonance width (Width function) derived in this section attempts to quantify the width of potentially unstable regions near each resonance line. In this region, the tune will start to oscillate, and eventually hit the resonance and lock-on. The derivation follows Chao's [14] resonance width Δ, which he derived for a sextupole perturbation. See figure 10.

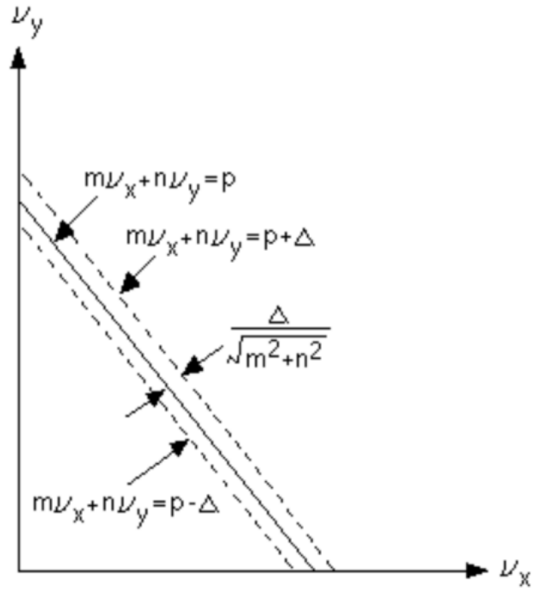

Figure 10: Resonance width in tune space (Figure 9.7 in [14])

Given a resonance line $m\nu_x + n\nu_y = p$, $(m\mu_x + n\mu_y = 2\pi p)$, Chao derives the width to be

$$\frac{\Delta}{\sqrt{m^2+n^2}} = \frac{1}{2\sqrt{m^2+n^2}}\left(\frac{m|m|}{A_x} + \frac{n|n|}{A_y}\right) A_x^{\frac{|m|}{2}} A_y^{\frac{|n|}{2}} |C_{abcd}| \tag{112}$$

such that $a - b = m$, $c - d = n$.

C_{abcd} are the four index Fourier coefficient of the following Fourier series, where the dependence on the actions have been factor out of the coefficients.

$$f(\phi_x, \phi_y) = \sum_{a,b,c,d} A_x^{\frac{|a-b|}{2}} A_y^{\frac{|c-d|}{2}} C_{abcd} e^{i(a-b)\phi_x} e^{i(c-d)\phi_y}. \tag{113}$$

The width is defined as the amplitude of oscillation of a particle's tune due to the resonance, as derived from a co-rotating Lie map.

Repeating Chao's derivation for the beam-beam map, we start we a general perturbation with a Fourier expansion. Let $e^{-:H:} = e^{:f_2:} e^{:h:}$ describe our system in its Normal form, where $f_2 = -\mu_x A_x - \mu_y A_y$, and h takes the form $h_0 + h^r$. h_0 does not contain oscillating terms; it can be absorbed into $f2$. h^r contains only one resonant term.

Let $m\mu_{x0} + n\mu_{y0} = 2\pi p$ be the resonant frequency. Consider a system near res-

onance with $\mu_x \approx \mu_{x0}$, $\mu_y \approx \mu_{y0}$, such that $m\mu_{x0} + n\mu_{y0} = 2\pi p + \epsilon$, for some small $\epsilon \approx 0$. Consider the following change to a co-rotating frame of resonant frequencies in action-angle coordinates:

$$\phi'_x = \phi_x + \mu_{x0}k, \quad \phi'_y = \phi_y + \mu_{y0}k \tag{114}$$

where k denotes the "turn index", such that k=1 corresponds to one full turn. The Lie map which generates this rotation is

$$R(k) = e^{:A_x\mu_{x0}k + A_y\mu_{y0}k:}. \tag{115}$$

The map after one turn in the co-rotating frame is therefore:

$$\begin{aligned} e^{-:H':} &= R(1)R(k)e^{-:H:}R(-k) \\ &= R(1)R(k)e^{:f_2:}R(-k)R(k)e^{:h:}R(-k) \\ &= (e^{:(k+1)(A_x\mu_{x0}+A_y\mu_{y0}):}e^{:f_2:}e^{:-k(A_x\mu_{x0}+A_y\mu_{y0}):})(e^{:k(A_x\mu_{x0}+A_y\mu_{y0}):}e^{:h:}e^{-:k(A_x\mu_{x0}+A_y\mu_{y0}):}). \end{aligned} \tag{116}$$

Since $R(k)$ commutes with $e^{:f_2:}$, the first term becomes $e^{:A_x\mu_{x0}+A_y\mu_{y0}}e^{:f_2:}$. Substituting in f_2, and combining exponents to find f'_2

$$\begin{aligned} e^{:A_x\mu_{x0}+A_y\mu_{y0}}e^{:f_2:} &= e^{:A_x(\mu_{x0}-\mu_x)+A_y(\mu_{y0}-\mu_y):} \\ &= e^{:f'_2:}. \end{aligned} \tag{117}$$

The second term in (116) is a simple rotation $\phi \to \phi'$.

$$\begin{aligned} e^{:k(A_x\mu_{x0}+A_y\mu_{y0}):}e^{:h:}e^{-:k(A_x\mu_{x0}+A_y\mu_{y0}):} &= e^{:h:'} \\ &= e^{:h'_0+C_{mn}e^{im\phi'_x+in\phi'_y}:}. \end{aligned} \tag{118}$$

The new eigenfunctions of $: f_2' :$ are $e^{im\phi_x'}e^{in\phi_y'}$. The eigenvalue equation is

$$\begin{aligned} : f_2' : e^{im\phi_x'}e^{in\phi_y'} &= -\frac{\partial e^{im\phi_x'}e^{in\phi_y'}}{\partial \phi_x'}\frac{\partial f_2'}{\partial A_x} - \frac{\partial e^{im\phi_x'}e^{in\phi_y'}}{\partial \phi_y'}\frac{\partial f_2'}{\partial A_y} \\ &= [im(\mu_{x0}-\mu_x) + in(\mu_{y0}-\mu_y)]e^{im\phi_x'}e^{in\phi_y'} \\ &= i\epsilon e^{im\phi_x'}e^{in\phi_y'}. \end{aligned} \tag{119}$$

Using BCH to find H',

$$H' = -f_2 - h_0 - c_{mn}\frac{i\epsilon}{1-e^{-i\epsilon}}e^{im\phi_x'}e^{in\phi_y'}. \tag{120}$$

In the co-rotating coordinate system, the resonant part is well behaved in the limit as $\epsilon \to 0$. I.e. it does not generate the small divisor problem which occurs in the static coordinate system;

$$\lim_{\epsilon \longrightarrow 0}\frac{i\epsilon}{1-e^{-i\epsilon}} = 1. \tag{121}$$

Substituting in the limit for small ϵ into (120), Hamilton's equations give the tune change with respect to turn number

$$\begin{aligned} \frac{d\phi_x'}{dk} &= \frac{\partial H'}{\partial A_x} = \mu_x - \mu_{x0} - \frac{\partial h_0}{\partial A_x} - \frac{\partial c_{mn}}{\partial A_x}e^{im\phi_x'}e^{in\phi_y'}. \\ \frac{d\phi_y'}{dk} &= \frac{\partial H'}{\partial A_y} = \mu_y - \mu_{y0} - \frac{\partial h_0}{\partial A_y} - \frac{\partial c_{mn}}{\partial A_y}e^{im\phi_x'}e^{in\phi_y'}. \end{aligned} \tag{122}$$

The resonance width (Width function) is then defined as the amplitude of oscillation of the term $\frac{1}{\sqrt{m^2+n^2}}(m\frac{d\phi_x'}{dk}+n\frac{d\phi_y'}{dk})$ due to the resonant term in h; this can be expressed in terms of derivatives of the standard Fourier coefficients,

$$\Delta = \frac{1}{\sqrt{m^2+n^2}}(m\frac{\partial C_{mn}}{\partial A_x} + n\frac{\partial C_{mn}}{\partial A_y}) \tag{123}$$

which reduces to Chao's sextupole formula for a sextupole case. We have absorbed the factor of $\frac{1}{\sqrt{m^2+n^2}}$ into the definition of Δ.

For a strictly vertical or horizontal resonance line, this has a simple interpretation. Suppose the resonance line is $m\mu_x = 2\pi p$, the particle's tune in the co-rotating coordinates $\frac{d\phi_x'}{dk}$ oscillates about the value $(\epsilon - \frac{\partial h_0}{\partial A_x})$ with amplitude Δ. Consider the

long-term behaviour after many turns; the tune eventually will hit the resonance line, and locks-on to the resonance, where it will then repeat its motion periodically. More generally, Δ can be seen as a 2D generalization of this amplitude. In the co-rotating coordinates, when $\Delta > \epsilon$, the particle exhibits resonant behaviour.

We note that for multiple perturbations at different phase shift, phase factors must be included. Comparing with (107), we sum over index k, which labels different beam-beam interactions.

$$\Delta = \sum_k \frac{1}{\sqrt{m^2+n^2}}(m\frac{\partial C_{mn}^{(k)}}{\partial A_x} + n\frac{\partial C_{mn}^{(k)}}{\partial A_y})e^{im\Delta\mu_x^{(k)}}e^{in\Delta\mu_y^{(k)}}. \tag{124}$$

Noting that action-angle transformation of a monomial term is of the form $a_n x^n \to a_n\sqrt{2A_x}^m \sin\phi_x{}^m$. Given some Taylor expansion in action-angle form, by expanding the sine powers into sine harmonic modes, it is possible to find the exact dependence of the Fourier coefficients on the action variable to obtain a formula that resembles Chao's.

$$\begin{aligned}
&\sum_{m,n=0} a_{mn}x^m y^n \\
&= \sum_{m,n=0} a_{mn}\sqrt{2A_x}^m\sqrt{2A_y}^n \sin\phi_x{}^m \sin\phi_y{}^n \\
&= \sum_{m,n=0} a_{mn}\sqrt{2A_x}^m\sqrt{2A_y}^n (\frac{i}{2})^{m+n}(e^{-i\phi_x}-e^{i\phi_x})^m(e^{-i\phi_y}-e^{i\phi_y})^n \\
&= \sum_{m,n=0} a_{mn}\sqrt{2A_x}^m\sqrt{2A_y}^n (\frac{i}{2})^{m+n}\sum_{k=0}^{m}\binom{m}{k}(-1)^k e^{i(m-2k)\phi_x}\sum_{l=0}^{n}\binom{n}{l}(-1)^l e^{i(n-2l)\phi_y}.
\end{aligned} \tag{125}$$

By collecting the desired harmonics, we obtain our Fourier coefficient as explicit functions of A_x and A_y. For fixed amplitude, it is simpler to compute the partial derivatives numerically, which was done for Width function plots in the next section.

6 Results

6.1 Verification of effective Hamiltonian against tracking

The effective Hamiltonian is to be interpreted as an (approximate) invariant of the system. Far away from resonance, in the regime where the approximation holds, tracking and the model should agree; tracked particles of a given action should lie on level curves/surfaces of the invariant. The approximation relies on the fact that potential-like terms in the perturbation can be properly approximated by a finite Fourier series, that the system is far enough away from resonances such that the effective Hamiltonian does not experience the small divisor problem, and that the perturbation is small enough such that a first order (in perturbation power) BCH suffices to combine maps.

For any function H, $\{H, H\} = 0$; H is conserved by maps generated by itself. This breaks down however at resonances, where singularities occur in the effective Hamiltonian, yet motion can remain stable.

For the purpose of verifying our effective invariant, "tracked" particles are compared with plots of the invariant. Particle motion is solved for turn by turn in Mathematica. The one-turn matrix map used by the Mathematica code was generated from MadX using real LHC data. The particle is plotted in phase space after each turn and is expected to lie on a level curve/surface of the invariant. The "tracking" is independent of the theory of "Lie maps"; tracking relies strictly on standard Hamiltonian mechanics.

In 4-D, the invariant defines a surface of constant A_x and A_y. Particles starting on the surface will remain on the surface. However, it is difficult to plot this. Instead, we will plot the planes $A_y = 0, A_x = A_{x0}$ and $A_x = 0, A_y = A_{y0}$, starting tracked particles in those respective planes.

For the purpose of this test, a 2 IR beam-beam model has been constructed. Each IR is comprised of 9 long-range interactions at a normalized separation of 12.5 σ, followed by a head on interaction, followed by 9 more long-range interactions mirroring the first set. The particle is initialized at a normalized amplitude $(a_x, a_y) = (6\ \sigma, 0)$ and $(a_x, a_y) = (0, 6\ \sigma)$, where $\sigma = 354\ \mu$m.

A discussion of the deviation from tracking can be found in the appendix F.

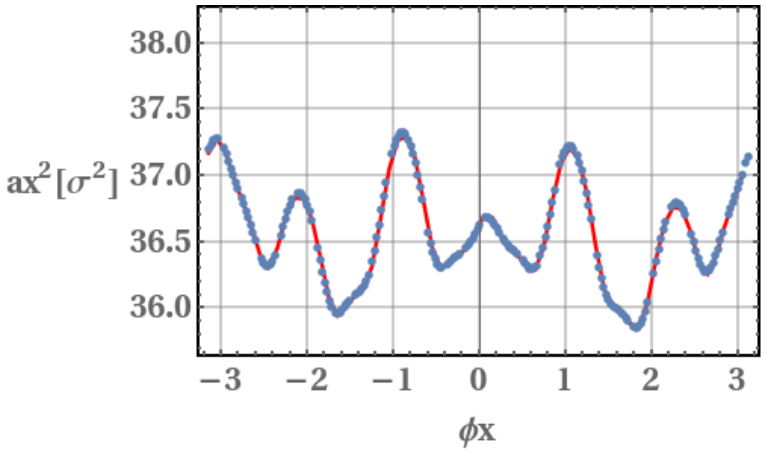

Figure 11: $a_y = 0$ tracked particle (blue) vs invariant curve (red) plot of normalized action $a_x^2[\sigma^2]$

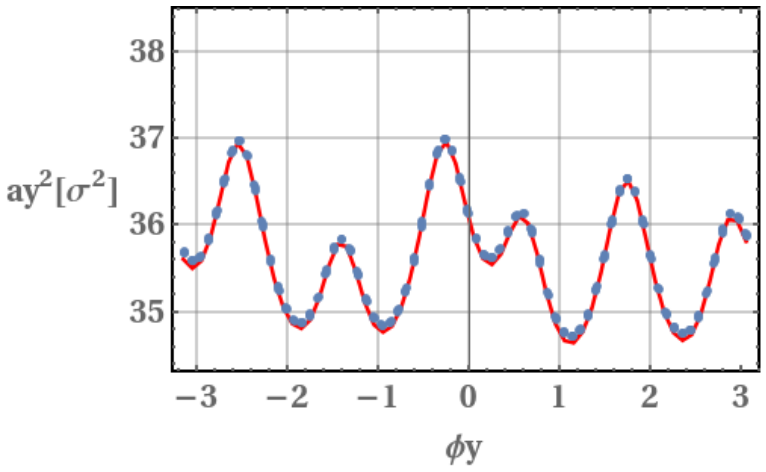

Figure 12: $a_x = 0$ tracked particle (blue) vs invariant curve (red) plot of normalized action $a_y^2[\sigma^2]$

6.2 Resonance cancelling by phasing

This was first studied in [40]. Consider the two dimensional effective Hamiltonian of a linear ring with two beam-beam interactions, phased by $\Delta\mu_1$ in μ_x and $\Delta\mu_2$ in μ_y. Suppose two beam-beam interactions have the same Fourier coefficients. Then the effective Hamiltonian $H = -F_{eff}$ may be written as

$$F_{eff} = f_2 + \sum_{m,n=-\infty}^{\infty} \frac{C_{mn}}{2\sin(\frac{m\mu_x}{2} + \frac{n\mu_y}{2})}[e^{im(\frac{\mu_x}{2}+\phi_x)+in(\frac{\mu_y}{2}+\phi_y)} + e^{im(\frac{\mu_x}{2}+\phi_x+\Delta\mu_1)+in(\frac{\mu_y}{2}+\phi_y+\Delta\mu_2)}]. \tag{126}$$

Given that C_{mn} are the Fourier coefficients of a real function (i.e. the beam-beam potential), we have the following symmetries: $C_{-mn} = C_{mn}$, $C_{m-n} = C_{mn}$. Then F_{eff} may be written as

$$F_{eff} = f_2 + \sum_{m,n=1}^{\infty} \frac{4C_{mn}}{2\sin(\frac{m\mu_x}{2} + \frac{n\mu_y}{2})}(\cos[m(\frac{\mu_x}{2} + \phi_x) + n(\frac{\mu_y}{2} + \phi_y)] + \cos[m(\frac{\mu_x}{2} + \phi_x + \Delta\mu_1) + n(\frac{\mu_y}{2} + \phi_y + \Delta\mu_2)]). \tag{127}$$

Using the sum of cosine identity, $\cos(a+b) + \cos(a) = 2\cos(a + \frac{b}{2})\cos(\frac{b}{2})$,

$$F_{eff} = f_2 + \sum_{m,n=1}^{\infty} \frac{4C_{mn}}{\sin(\frac{m\mu_x}{2} + \frac{n\mu_y}{2})}(\cos[m(\frac{\mu_x}{2} + \frac{\Delta\mu_1}{2} + \phi_x) + n(\frac{\mu_y}{2} + \frac{\Delta\mu_2}{2} + \phi_y)] \times \cos[m\frac{\Delta\mu_1}{2} + n\frac{\Delta\mu_2}{2}]). \tag{128}$$

Suppose $m\mu_x + n\mu_y = 2\pi p$ is resonant, i.e. $\sin(\frac{m\mu_x}{2} + \frac{n\mu_y}{2}) = 0$. Then there exists values of $\Delta\mu_1$ and $\Delta\mu_2$ which cancels out the resonance. Taylor expanding the sine about $p\pi$,

$$\sin(\frac{m\mu_x}{2} + \frac{n\mu_y}{2}) = (p\pi - (\frac{m\mu_x}{2} + \frac{n\mu_y}{2})) - 1/6(p\pi - (\frac{m\mu_x}{2} + \frac{n\mu_y}{2}))^3 + O(\epsilon^5). \tag{129}$$

Let q be an odd integer, expanding the cosine about $q\frac{\pi}{2}$.

$$\cos(m\frac{\Delta\mu_1}{2} + n\frac{\Delta\mu_2}{2}) = (q\frac{\pi}{2} - (\frac{m\Delta\mu_1}{2} + \frac{n\Delta\mu_2}{2})) - 1/6(q\frac{\pi}{2} - (\frac{m\Delta\mu_1}{2} + \frac{n\Delta\mu_2}{2}))^3 + O(\epsilon^5). \tag{130}$$

Clearly, if both the cosine and the sine are taken to their respective zeros at the same

rate, the denominator and the numerator cancel out.

$$\lim_{\delta \to\ 1} \frac{\cos\left(\frac{q\pi}{2} - \delta\frac{q\pi}{2}\right)}{\sin\left(p\pi - \delta p\pi\right)} = 1. \tag{131}$$

Therefore, the resonance cancelling condition is

$$m\Delta\mu_1 + n\Delta\mu_2 = \pi q \quad \text{for odd q.} \tag{132}$$

Namely, if $\Delta\mu_1 = \Delta\mu_2 = \frac{\pi}{2}$, then for odd integers q, resonance of order $2q$ will be cancelled.

For head-on beam-beam interactions, the evaluation of the invariant leaves some visual artifacts (extremely weak resonance lines which are invisible in the Width function plots manifest as white dots in the invariant plots). The resonance cancellation can be more easily seen using the Width function. The 13th order resonances do not appear in head-on interactions as expected. When two head-on interactions are phased by an integer multiple of $\frac{\pi}{2}$, the 10th order resonances disappear. Since the system is periodic in 2π, it is expected that any phase shift of $2n\pi + \frac{\pi}{2}$ will result in cancellations of resonances of even orders non-divisible by 4 (6,10,14,18 etc...) from inspecting (132).

The cancellation for a 2 impulse head-on beam-beam toy model is shown in the appendix G.23.

6.2.1 Idealized head-on/long-range combined model phased for resonance cancellation

The 10th order resonance cancellation via $\frac{\pi}{2}$ phasing was also verified on a more "realistic" model consisting of both long-range and head-on interactions. The model consists of 2 IRs, each comprised of 12 long-range interactions at a normalized separation of 12.4 σ, followed by a head-on interaction, followed by 12 more long-range interactions. The long-range interactions are phased by π across the interaction point of an IR. The two interaction regions are phased by 65.5π. 10th order as well as 6th order resonances diminished. The added complexity did not interfere with the validity of (Figure 6.2). The plots can be found in the appendix G.24.

6.2.2 Resonance cancelling tolerance

Realistically, the optics can only be tuned to a finite accuracy; the phase shift cannot be at exact values such as $\frac{\pi}{2} + 2n\pi$. A test in tolerance was performed by plotting the Width function and the Invariant at different deviations from an idea phase shift to estimate roughly what phase shift precision is required for cancellations.

The beam-beam setup is the idealized model from previous sections, with 2 IRs, 25 interactions per IR. The working point in this section was changed to the HL-LHC suggested value of (62.31, 60.32). Using this setup, the two IRs were phased to $64\pi + \frac{\pi}{2}$. Four plots were generated, using deviations of $2\pi 10^{-4}, 2\pi 10^{-3}, \pi 10^{-2}, 2\pi 10^{-2}$ in both μ_x and μ_y.

At $2\pi 10^{-4}$ and $2\pi 10^{-3}$ away from ideal phasing, there was significant weakening of the 10th order resonance. An interesting feature at $2\pi 10^{-4}$ is the increase of 16th order resonance width. Once the deviation from idea phase shift is around $5{*}10^{-}3{*}2\pi$, the resonance cancellation is no longer significant. The figures can be found in the appendix G.25.

6.3 Beam-beam resonances of HL-LHC and resonance cancellation

In contrast to previous sections which simplified models mimicking the beam-beam setup of the HL-LHC, this section uses bunch information and phase shifts generated from the HL-LHC lattice, computed using MadX. We examine the beam-beam resonances from two interaction regions, IR1 and IR5. The beam-beam setup includes 70 individual interactions, each computed up to 16 Fourier terms. There are 70 interactions per interaction region. Each region consists of one head-on, and 34 long-range interactions. There is a phase advance of $\approx \pi$ across the interaction point. The phase advance between the head-on interactions of the two interaction regions is $31.207 * 2\pi$ in x, and $30.370 * 2\pi$ in y. The bunch data are plotted (5), and tabulated (A).

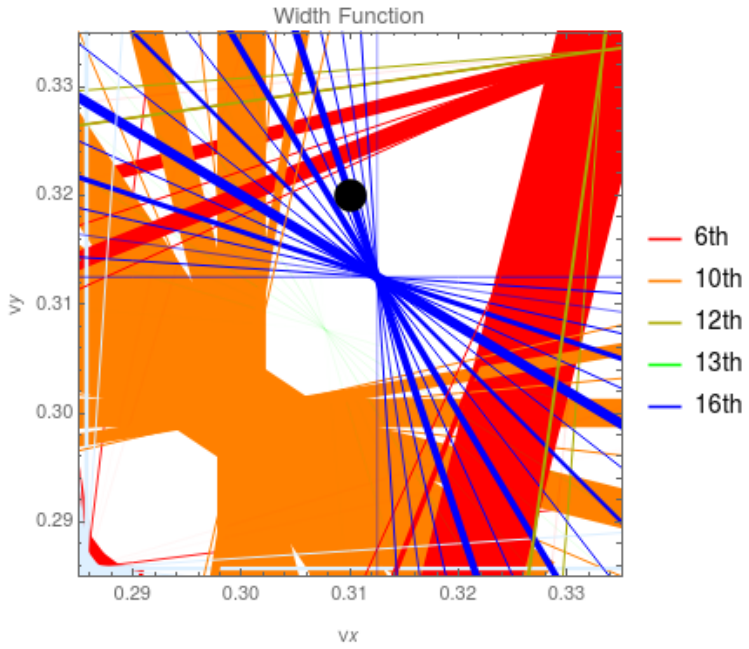

Figure 13: 70 impulse IR1-IR5 model Width function with no phasing: order 6(red), 10(orange), 13(green), 16(blue)

Figure 13 shows that the 10th order (orange) resonances is quite significant with the given phases. The black disk denotes the location of the working point. Its size is not representative of tune smear. Note that the working point lies on (or very close to) a 16th order resonance line; it is likely non-optimal.

Figure 14 shows the Invariant (effective Hamiltonian) plot of the same beam-beam setup; the same resonances are visible. The dotted lines represent thin resonance lines, the filled lines represent thicker resonances. Since the working point lies above the main diagonal, only half the space is plotted for efficiency.

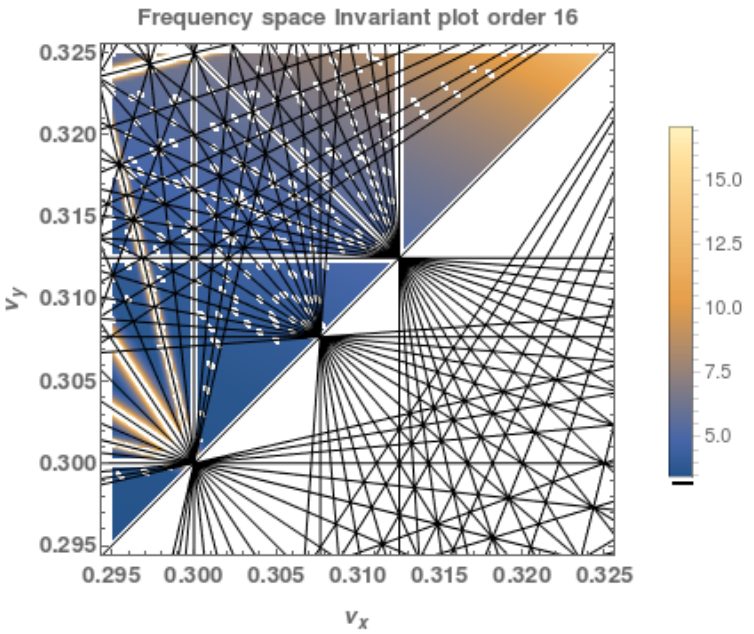

Figure 14: 70 impulse IR1-IR5 model beam-beam Invariant(effective Hamiltonian) plot. Scale in $[\sigma^2]$.

6.3.1 10th order resonance cancelling

By shifting all the IR5 bunches by 0.043 in ν_x and -0.12 in ν_y, 10th order resonances can be reduced in strength. This brings both the vertical and horizontal phase shifts between the 2 IRs to a value close to $\frac{\pi}{2} + 2\pi n$. This particular phase shift also cancels out any resonances of even order which are non-divisible by 4, e.g. 6, 14.

See figure 15, which has the same beam-beam configuration as figure 13, but with IR5 shifted by the aforementioned amount. There is noticeable cancellation of the 10th order resonance.

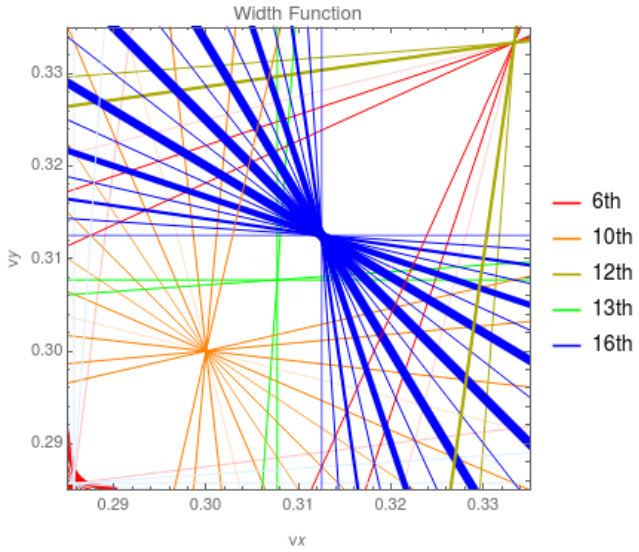

(a) HL-LHC 70 BB: 10th order correction

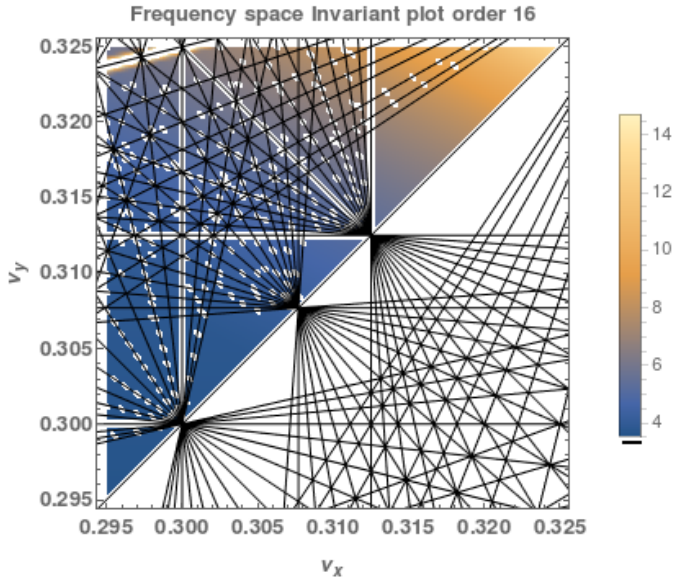

(b) HL-LHC 70 BB: 10th order (orange) correction invariant. Scale in σ^2.

Figure 15: 70 impulse IR1-IR5 model 10th order resonance reduction $\Delta\mu_x = 0.043(2\pi)$, $\Delta\mu_y = -0.12(2\pi)$.

6.3.2 16th order resonance cancelling

The tentative working point of the HL-LHC 62.31, 60.32. The closest resonance cluster is the 16th order. By inspection of equation (132), a phase advance of $\frac{\pi}{16}$ between

IRs satisfies the resonance cancellation condition for 16th order. Figure 16 show this cancellation, contrasted with figure 13. Applying a phase shift of $2\pi(-0.17535)$ in μ_x and $2\pi(-0.33835)$ in μ_y to the standard HL-LHC bunch phasing (Figure 13), the phase advance from IP to IP is brought to $2n\pi + \frac{\pi}{16}$.

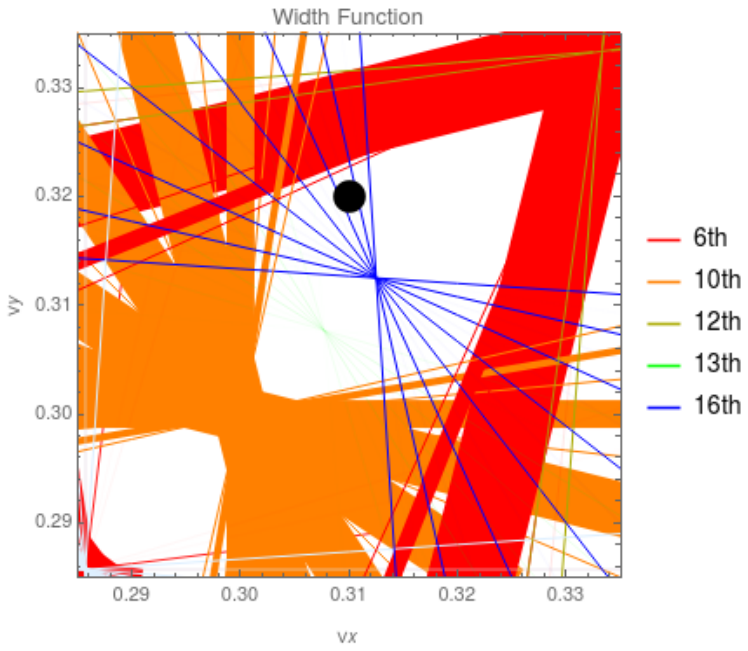

Figure 16: 70 impulse IR1-IR5 model 16th order (blue) resonance reduction $\Delta\mu_x = -0.17535(2\pi)$, $\Delta\mu_y = -0.33835(2\pi)$

One should note that the cancellation is even more powerful than the figure suggests; the actual width Δ of 16th order resonance lines is lowered by a factor of ≈ 50 by this phasing. For example, the width of the $16\mu_x = 10\pi$ line is reduced from $1.98 * 10^{-14}$ to $4.30 * 10^{-16}$ times the horizontal plot range.

6.3.3 General procedure for arbitrary resonance order

For a resonance line of order $m + n = q$, a phase shift between IP of $\Delta\nu_x = \frac{1}{2q} = \Delta\nu_y$ (or phase shift of $\Delta\mu_x = \frac{\pi}{q} = \Delta\mu_y$) satisfies the resonance cancelling condition (132).

For example, $4\mu_x - 10\mu_y$ defines a single resonance line close to the working point. It is a 6th order resonance which clusters outside of our region of interest. Nonetheless, this line appears relatively close to our working point. Solving for the resonance cancelling equation, we find that a phase shift of $\frac{-\pi}{6}$ or $\frac{11\pi}{6}$ is a solution.

By phasing the second IR from the first one by $\Delta\mu_x = 2\pi(-0.2066 - 1/12)$, and $\Delta\mu_y = 2\pi(-0.3696 - 1/12)$, bringing the total phase shift from IR to IR to $2k\pi - \frac{\pi}{6}$, the $4\mu_x - 10\mu_y$ resonance line is cancelled. See figure 17, where the thick red resonance line above the working point has been significantly thinned. Note that this resonance is a stable one, this was purely done as a demonstration of the theory.

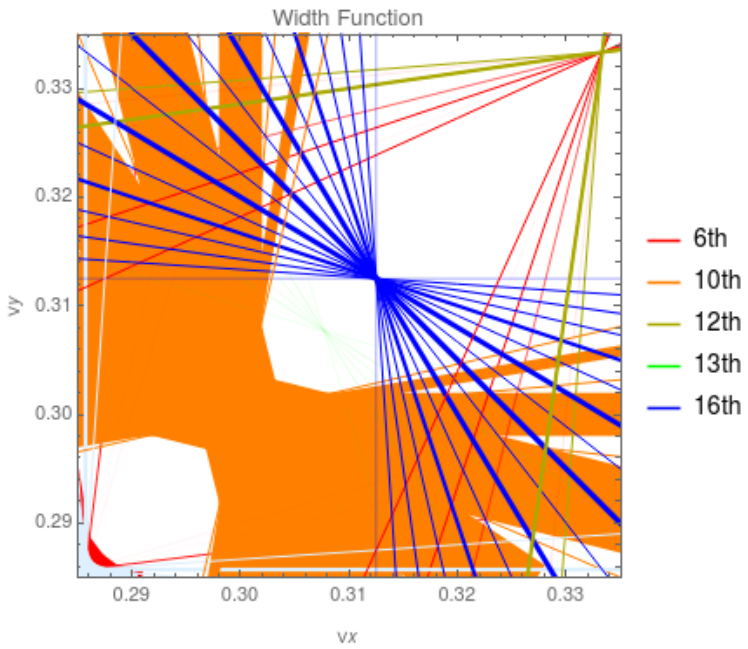

Figure 17: 70 impulse IR1-IR5 model Width function with order 6 cancellation via phase shift

6.4 Alternative working point

The alternate working point of $(0.475, 0.485)$, close to half integer resonance, has been suggested by [7] based on numerical simulations.

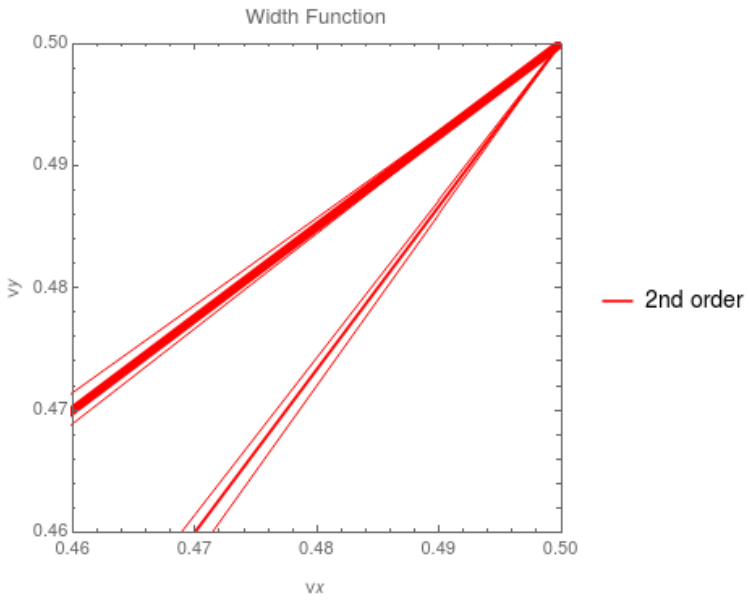

Figure 18: 70 impulse IR1-IR5 model Width function plot near new working point (0.475,0.485)

Figure 18 show the Width function near $(0.475, 0.485)$. When plotting the standard Width function from for orders $5-32$, the region is empty. Resonances of orders $2-4$ were included in the Figure. There are two visible groupings of resonance lines with positive slope; these are stable "difference" resonances. There seem to be ample empty space in this region, allowing for more working points far from dangerous resonances.

It seems that the new working is ideal by virtue of non-proximity to thick "sum" resonance lines. When comparing against tracking, the invariant(s) show a resonant behaviour, perhaps due to the proximity of low order "difference resonance" resonance. The stability of tracked particles confirms that the resonance is not dangerous. (This comparison can be found in the Appendix G.29-G.30)

6.5 The effect of crossing angle on HL-LHC beam-beam resonances

The crossing angle is an important parameter to be considered for the HL-LHC. It affects the luminosity (57) via the its effect on long-range beam-beam and on the Piwinski angle (58). From (54) and (55), the normalized separation is proportional to the crossing angle

$$d \approx [1 + \sqrt{\frac{\beta_{y,x}(s)}{\beta_{x,y}(s)}}]\frac{\Theta_c}{2}\sqrt{\frac{\beta^*}{\epsilon}}. \tag{133}$$

The HL-LHC beam-beam model used in this section is the same as Fartoukh's [25]; the same lattice was imported into MadX to generate bunch data. Although our model does not depend explicitly on crossing angle, it does depend on it implicitly via normalized separations. The default crossing angle value is taken from [25].

Figure 19 show Width function plots with different crossing angles[8]. The crossing angles were set to $\frac{1}{2}$, $\frac{2}{3}$, $\frac{3}{2}$, and 3 times the value of 590 μrad by adjusting the normalized distances.

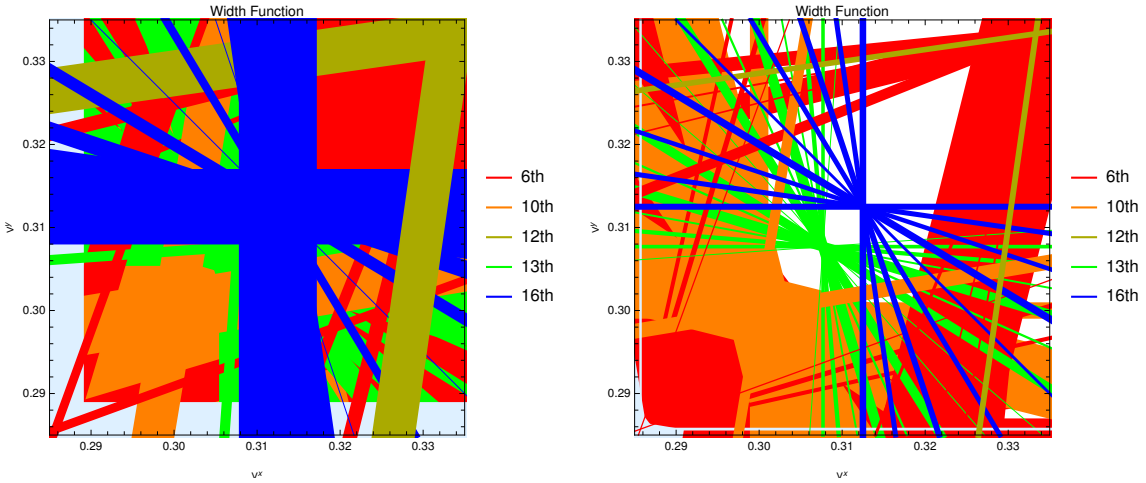

(a) 2 IR HL-LHC ($\frac{1}{2}590 = 295$) μrad crossing angle

(b) 2 IR HL-LHC 393 ($\frac{2}{3}590 \approx 393$) μrad crossing angle

[8]The corresponding Invariant plots can be found in the Appendix G.27.

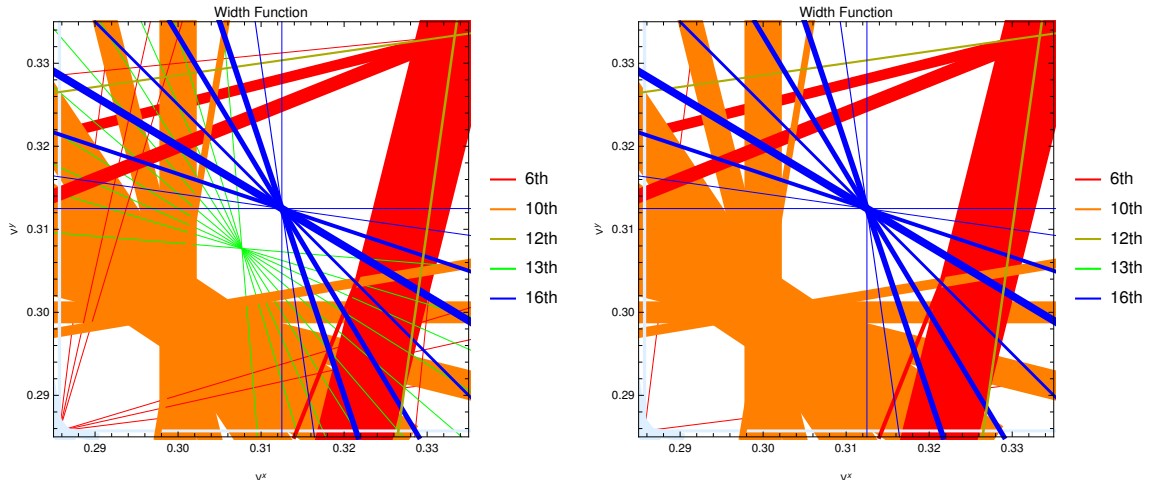

(c) 2 IR HL-LHC ($\frac{3}{2}590 = 885$) μrad crossing angle

(d) 2 IR HL-LHC ($3 * 590 = 1770$) μrad crossing angle

Figure 19: 70 impulse IR1-IR5 model Width function plot with varying crossing angles: 6th order(red), 10th order(orange), 13th order(green), 16th order(blue)

At 295 μrad, beam-beam resonances are significant. The 10th order resonances dominate, but the 10th and 13th order resonances are also non-negligible. The Width function fill the space.

At 393 μrad, the effect of all beam-beam resonances is reduced. The 13th order resonances are visibly more powerful than at 590 μrad, but the 16th and 10th order ones of similar width.

At 885 μrad, all resonances look similar compared to 590 μrad.

At 1770 μrad, the 10th and 16 order resonances look similar 590 μrad. However, the 13th order resonances, which are strictly due to long-range beam-beam have disappeared.

The disappearance of 13th order, and invariance of the 10th and 16th order at very high crossing angle suggested that the 10th and 16th order resonances are mainly caused by head-on interactions. At 1770 μrad, the normalized distances are of the order of 35, the long-range beam-beam potential are completely negligible. However, the current working point sits close to the 16th order resonances, which seemingly was not minimized by increasing the crossing angle past 590μrad.

The similarity of Width functions at 590 μrad and 1770 μrad suggest not much improvement on beam-beam resonances can be made at the current working point

by increasing the crossing angle past 590 μrad, even by a factor of 3. 590 μrad is close to the ideal crossing angle for the purpose of minimizing beam-beam resonances with the given bunch and IP phasing. On the contrary, increasing the crossing angle decreases the Piwinski angle and negatively affects luminosity; too large a crossing angle is counter-productive.

7 Summary and Conclusion

This thesis investigated beam-beam interactions and their resonances using a model with multiple beam-beam impulses coupled to a harmonic oscillator type one-turn map using Lie algebraic methods. An effective Hamiltonian for a one-turn map coupled to 70 beam-beam impulses was computed and plotted in tune space to study beam-beam resonances. The effective Hamiltonian was shown to agree with numerical tracking away from resonance. A width formula was developed for resonance lines.

It was shown that it is possible to weaken or even remove resonances of certain orders by using the appropriate phasing of beam-beam impulses between IRs. This is verified against the effective Hamiltonian and the width formula. These tools were used to study the resonances close to the suggested working point of the HL-LHC as well as a new working point suggested by a previous study. The effects of changing separations (crossing angles) was also briefly studied.

Head-on beam-beam interactions drive even order resonances. Long-range beam-beam interactions drive resonances of all orders. These resonances densely populate the space of tunes; they are specified by the equations $m\mu_x + n\mu_y = 2\pi q$, for all integers m, n, q, where q denotes the order of the resonance. Resonances of the same order intersect the main diagonal, defined by $\mu_x = \mu_y$, at the same location (Figure 8). Although resonance lines densely populate the frequency space, in general, the importance and width of a resonance rapidly decreases as its order increases. The working point of the HL-LHC is $(\nu_x, \nu_y) = (60.31, 62.32)$. The closest resonances (of order less than 32) are of 16th and 6th order (Figure 13).

These resonances can be analyzed using Lie algebraic methods. A Lie map is constructed for beam-beam interactions, the generator F_{eff} (107) is constructed using the BCH formula. The generator or effective Hamiltonian $H_{eff} = -F_{eff}$ is singular precisely at a resonance line. H_{eff} is plotted (Invariant plots, see Appendix figure 14) as a function of tunes to study resonances. More important (wider) resonances are assumed to experience more powerful singularities; these will be visually distinguishable in the plot as thicker lines.

A resonance width formula (Width function 124), representing the lock-on width of a resonance, has been derived following Chao's work [14]. With beam-beam in mind, the formula was derived to include phase factors and Fourier coefficients of arbitrary orders. Plotting (Figure 13) this function arguably gives a clearer picture

of resonances when compared with Invariant plots.

The beam-beam model used in this thesis treats each bunch as an impulse. 70 beam-beam impulses (table A) are included, with 35 per interaction regions. At the centre of each interaction region is a head-on interaction. The rest of the impulses are long-range ones, approximately at a normalized distance of 12.5 σ. By changing the phase between IRs, some resonances can be cancelled; this follows from the effective Hamiltonian and simple trigonometry (Section 6.2). Cancellation via phasing for a resonance of order q occurs when the phase advance from one IR to the next in both x and y is $\frac{\pi}{k}$, if $\frac{q}{k}$ is odd. So a resonance of order q can always be cancelled by by a phase shift of $\frac{\pi}{q}$, and some special phase advances can cancel multiple resonances. This phase advance needs not be exact; a $2\pi(10^{-4})$ deviation from the exact fraction offers excellent cancellation, and a $2\pi(10^{-3})$ still offers reasonable cancellation for resonances of order 10.

Section 6.3.1 shows that a phase advance of $\frac{\pi}{2}$ reduces the 10th order resonances, as well as the 6th order resonances near the working point. Section 6.3.2 show the reduction of 16th order resonances which is dangerously close to the working point with a phase advance $\frac{\pi}{16}$. At the suggested working point of $(62.31, 60.32)$ and crossing angle of 590 μrad, a phase advance of $\frac{\pi}{16}$ is recommended to lessen the effects of 16th order beam-beam resonances close to the working point.

Section 6.4 tests a working point $(0.475, 0.485)$, near the half-integer resonances, suggested by Furuseth [7], based on numerical simulations. The region around the working point lacks dangerous resonance lines and seems to be ideal for the purpose of minimizing the impact of beam-beam resonances. However, the comparison of the Invariant in phase space in action-angle coordinates against tracking show a resonant behaviour in the invariant which is not seen by the tracking, further investigation in this region is recommended.

Section 6.5 shows the effect of changing the crossing angle on resonances. At a low crossing angle of 295 μrad, the beam-beam resonances completely dominate the tune space. By increasing the crossing angle all resonances decrease. The 13th order resonances eventually disappear, but the 10th and 16th order remain. The 13th order resonances are strictly due to long-range interactions. The 10th and 16th order resonances are due to a combination of head-on and long-range interactions. At extremely large crossing angles, the long-range interactions become completely negligible, but the head-on interactions do not change. The crossing angle could be

slightly decreased to increase luminosity if the 16th order resonances are removed by phasing the IRs.

References

[1] G. Arduini et al. "High Luminosity LHC: challenges and plans". In: *JINST* 11.12 (2016), p. C12081. DOI: 10.1088/1748-0221/11/12/C12081.

[2] *High Luminosity LHC*. URL: https://home.cern/science/accelerators/high-luminosity-lhc. (accessed: 03.01.2019).

[3] A. J. Dragt. *Lie Methods for Nonlinear Dynamics with Applications to Accelerator Physics*. University of Maryland, 2019. URL: https://www.physics.umd.edu/dsat/dsatliemethods.html.

[4] *Computing with BOINC*. URL: https://boinc.berkeley.edu/trac/wiki/BoincOverview. (accessed: 06.26.2019).

[5] A. Poyet. "Compensation of the Long-Range Beam-Beam Interaction in the LHC". Presented 07 Sep 2017. Sept. 2017. URL: https://cds.cern.ch/record/2320490.

[6] W. Herr and D. Kaltchev. "Effect of phase advance between interaction points in the LHC on the beam-beam interaction". In: *LHC Project Report 1082*. May 2008. URL: https://cds.cern.ch/record/1103471/files/lhc-project-report-1082.pdf.

[7] S. V. Furuseth and X. Buffat. "Modeling of nonlinear effects due to head-on beam-beam interactions". In: *Phys. Rev. Accel. Beams* 21 (8 Aug. 2018), p. 081002. DOI: 10.1103/PhysRevAccelBeams.21.081002. URL: https://link.aps.org/doi/10.1103/PhysRevAccelBeams.21.081002.

[8] V. Kain. "Beam Dynamics and Beam Losses - Circular Machines". In: *Proceedings, 2014 Joint International Accelerator School: Beam Loss and Accelerator Protection: Newport Beach, CA, USA, November 5-14, 2014*. 2016, pp. 21–38. DOI: 10.5170/CERN-2016-002.21. arXiv: 1608.02449 [physics.acc-ph].

[9] K. Steffen. "Basic course on accelerator optics". In: *CAS CERN Accelerator School*. Vol. 1. 1984, pp. 25–54. URL: http://cdsweb.cern.ch/record/164925/files/CERN-85-19-V-1.pdf.

[10] E. W. Weisstein. *Cauchy Riemann Equations*. URL: http://mathworld.wolfram.com/Cauchy-RiemannEquations.html. (accessed: 02.017.2019).

[11] L. W. Casperson. "Solvable Hill equation". In: *Phys Rev. A* 30 (Nov. 1984), pp. 2749–2751. DOI: 10.1103/PhysRevA.30.2749.

[12] R. C. Manzano X. C. Vidal. *LHC layout, Taking a closer look at the LHC*. URL: https://www.lhc-closer.es/taking_a_closer_look_at_lhc/0.lhc_layout. (accessed: 02.05.2019).

[13] S. Dowdell et al. "Monte Carlo study of the potential reduction in out-of-field dose using a patient-specific aperture in pencil beam scanning proton therapy". In: *Physics in medicine and biology* 57 (Apr. 2012), pp. 2829–42. DOI: 10.1088/0031-9155/57/10/2829.

[14] A. Chao. *Lecture Notes on Topics in Accelerator Physics*. SLAC, 2002. URL: http://inspirehep.net/record/595287/files/slac-pub-9574.pdf.

[15] A. J. Lichtenburg and M. A. Liberman. *Regular and Stochastic Motion*. Applied Mathematical Sciences. Springer-Verlag, 1983. ISBN: 0-387-90707-6.

[16] S. N. Rasband. "The Poincare Map". In: *Chaotic Dynamics of Nonlinear Systems*. Wiley, 1990. Chap. 5.3. ISBN: 978-0471184348.

[17] E. S. Cheb-Terrab and H. P. de Oliveira. "Poincaré sections of Hamiltonian systems". In: *Computer Physics Communications* 95 (June 1996), pp. 171–189. DOI: 10.1016/0010-4655(96)00032-X. arXiv: gr-qc/9512042 [gr-qc].

[18] G. Guignard. "Phase space dynamics". In: *Frontiers of Particle Beams*. Ed. by M. Month and S. Turner. Vol. 296. Lecture Notes in Physics, Berlin Springer Verlag. 1988, pp. 1–50. DOI: 10.1007/BFb0031488.

[19] R Bruce et al. "Reaching record-low β^* at the CERN Large Hadron Collider using a novel scheme of collimator settings and optics". In: *Nuclear Instruments and Methods in Physics Research Section A: Accelerators, Spectrometers, Detectors and Associated Equipment* 848 (Dec. 2016). DOI: 10.1016/j.nima.2016.12.039.

[20] W. Herr. "Beam-Beam Effects". In: *CAS CERN Accelerator School*. 2005. URL: https://cas.web.cern.ch/sites/cas.web.cern.ch/files/lectures/trieste-2005/herr-beambeam.pdf.

[21] B. Houssais. Thesis, University of Rennes. 1967.

[22] Eberhard K. "Beam-beam dynamics". In: CERN-SL-94-78-AP (Sept. 1994), 16 p. DOI: 10.5170/CERN-1995-006.539. URL: https://cds.cern.ch/record/269336.

[23] W. Herr. "Beam-beam interactions". In: *CAS CERN Accelerator School*. 2006, pp. 379–410. DOI: 10.5170/CERN-2006-002.379.

[24] D. Kaltchev. "Fourier Coefficients of Long-Range Beam-Beam Hamiltonian via Two-Dimensional Bessel functions". In: *Proceedings, 9th International Particle Accelerator Conference (IPAC 2018): Vancouver, BC Canada*. 2018, THPAK108. DOI: 10.18429/JACoW-IPAC2018-THPAK108.

[25] S. Fartoukh et al. "Compensation of the long-range beam-beam interactions as a path towards new configurations for the high luminosity LHC". In: *Phys. Rev. ST Accel. Beams* 18 (12 Dec. 2015), p. 121001. DOI: 10.1103/PhysRevSTAB.18.121001. URL: https://link.aps.org/doi/10.1103/PhysRevSTAB.18.121001.

[26] W. Fischer et al. "Observation of strong-strong and other beam-beam effects in RHIC". In: vol. 1. June 2003, 135–137 Vol.1. ISBN: 0-7803-7738-9. DOI: 10.1109/PAC.2003.1288861.

[27] X. Buffat et al. "Coherent beam-beam mode in the LHC". In: *Proceedings, ICFA Mini-Workshop on Beam-Beam Effects in Hadron Colliders (BB2013): CERN, Geneva, Switzerland, March 18-22 2013*. 2014, pp. 227–230. DOI: 10.5170/CERN-2014-004.227. arXiv: 1410.5695 [physics.acc-ph].

[28] J. Qiang et al. "Recent advances of strong strong beam beam simulation". In: *Nuclear Instruments and Methods in Physics Research A* 558 (Mar. 2006), pp. 351–355. DOI: 10.1016/j.nima.2005.11.045.

[29] T. Pieloni. "A study of beam-beam effects in hadron colliders with a large number of bunches". Presented on 4 Dec 2008. 2008. URL: http://cds.cern.ch/record/1259906.

[30] M. Albert et al. "Head-on beam-beam collisions with high intensities and long range beam-beam studies in the LHC". In: (July 2011). URL: http://cds.cern.ch/record/1368896.

[31] W. Herr. "Effects of PACMAN bunches in the LHC". In: LHC-Project-Report-39. CERN-LHC-Project-Report-39. Geneva, July 1996. URL: https://cds.cern.ch/record/314386.

[32] D. Ritson and W. Chou. "Minimizing the pacman effect". In: 1997. DOI: 10.2172/563144.

[33] W. Herr. "Beam-beam issues in the LHC and relevant experience from the SPS proton anti-proton collider and LEP". In: *Conf. Proc.* C0106258 (2001), p. 001. URL: http://inspirehep.net/record/564871/files/001.pdf.

[34] Keenan. *Illustrating Lie Groups*. URL: http://keenan.is/illustrating/2017/03/03/illustrating-lie-groups/. (accessed: 06.20.2019).

[35] J. S. Bell. "Hamiltonian Mechanics". In: *CAS CERN Accelerator School*. Vol. 1. 1987, pp. 5–37. URL: http://cdsweb.cern.ch/record/179307/files/CERN-87-03-V-1.pdf.

[36] A. Kuppers. *Lectures on Diffeomorphism Groups of Manifolds*. University Lecture Notes. 2019. URL: http://www.math.harvard.edu/~kupers/teaching/272x/book.pdf.

[37] B. Hall. "The Baker-Campbell-Hausdorff Formula and Its Consequences". In: *Lie Groups, Lie Algebras, and Representations*. Graduate Texts in Mathematics. Springer, 2015. Chap. 5, pp. 109–137. ISBN: 978-3-319-13467-3.

[38] D. Kaltchev et al. "Extended-Domain Tune-Scans for the HL-LHC Dynamic Aperture in Presence of Beam-Beam Effects". In: *Proceedings, 9th International Particle Accelerator Conference (IPAC 2018): Vancouver, BC Canada, April 29-May 4, 2018*. 2018, TUPAL064. DOI: 10.18429/JACoW-IPAC2018-TUPAL064.

[39] T. Collins. "Resonances and Resonance Width". In: *Fermilab Tech Report*. May 1986. URL: https://lss.fnal.gov/archive/test-tm/1000/fermilab-tm-1405.pdf.

[40] W. Herr and D. Kaltchev. "Effect of phase advance between interaction points in the LHC on the beam-beam interaction". In: *LHC Project Report 1082*. 2008. URL: https://cds.cern.ch/record/1103471/files/lhc-project-report-1082.pdf.

8 Appendix

A Table of IR5 interaction point bunch data

Table of IP5 Bunch data					
Bunch name	Normalized d_x	Normalized d_y	Phase ν_x	Phase ν_y	Ratio $\frac{\sigma_x}{\sigma_y}$
BBIP5PL15	−14.0055	0	14.8491	14.2611	0.8
BBIP5PL14	−11.8394	0	14.8492	14.2612	1.1
BBIP5PL13	−10.2626	0	14.8492	14.2612	1.53
BBIP5PL12	−9.5243	0	14.8492	14.2613	1.86
BBIP5PL11	−9.23322	0	14.8493	14.2614	2.04
BBIP5PL10	−9.30368	0	14.8493	14.2616	1.98
BBIP5PL9	−9.97595	0	14.8493	14.2617	1.63
BBIP5PL8	−11.1004	0	14.8494	14.2618	1.25
BBIP5PL7	−12.0541	0	14.8495	14.262	1.05
BBIP5PL6	−12.4064	0	14.8497	14.2621	0.99
BBIP5PL5	−12.4061	0	14.8499	14.2623	0.99
BBIP5PL4	−12.4057	0	14.8502	14.2626	0.99
BBIP5PL3	−12.4049	0	14.8507	14.2631	0.99
BBIP5PL2	−12.403	0	14.8517	14.2641	0.99
BBIP5PL1	−12.3947	0	14.8549	14.2672	0.99
BBIP5L2	−4.23838	0	15.0427	14.4536	1.01
BBIP5L1	−1.69333	0	15.0764	14.488	1.01
BBIP5	0	0	15.0983	14.5102	1.01
BBIP5R1	1.69004	0	15.12	14.5322	1.
BBIP5R2	4.21887	0	15.1535	14.5658	1.
BBIP5PR1	12.386	0	15.3393	14.7456	0.99
BBIP5PR2	12.3978	0	15.3425	14.7487	0.99
BBIP5PR3	12.4008	0	15.3435	14.7497	0.99
BBIP5PR4	12.4022	0	15.344	14.7502	0.99
BBIP5PR5	12.403	0	15.3444	14.7505	0.99
BBIP5PR6	12.4036	0	15.3446	14.7507	0.99
BBIP5PR7	12.7776	0	15.3447	14.7508	0.93
BBIP5PR8	14.0589	0	15.3448	14.7509	0.78
BBIP5PR9	16.4013	0	15.345	14.751	0.6
BBIP5PR10	18.6997	0	15.3451	14.751	0.49
BBIP5PR11	19.0769	0	15.3452	14.7511	0.48
BBIP5PR12	18.0177	0	15.3454	14.7511	0.52
BBIP5PR13	15.9222	0	15.3454	14.7511	0.64
BBIP5PR14	13.2553	0	15.3455	14.7512	0.89
BBIP5PR15	11.3736	0	15.3455	14.7512	1.22

B Table of IR1 interaction point bunch data

Table of IP1 Bunch data					
Bunch name	Normalized d_x	Normalized d_y	Phase ν_x	Phase ν_y	Ratio $\frac{\sigma_x}{\sigma_y}$
BBIP1PL15	0	−11.257	46.0653	44.6323	0.79
BBIP1PL14	0	−13.143	46.0653	44.6324	1.09
BBIP1PL13	0	−15.804	46.0654	44.6324	1.51
BBIP1PL12	0	−17.8993	46.0654	44.6325	1.84
BBIP1PL11	0	−18.9677	46.0654	44.6326	2.02
BBIP1PL10	0	−18.6099	46.0654	44.6328	1.96
BBIP1PL9	0	−16.3384	46.0655	44.6329	1.61
BBIP1PL8	0	−14.005	46.0656	44.633	1.24
BBIP1PL7	0	−12.7286	46.0657	44.6332	1.04
BBIP1PL6	0	−12.356	46.0658	44.6333	0.98
BBIP1PL5	0	−12.3554	46.066	44.6335	0.98
BBIP1PL4	0	−12.3547	46.0664	44.6338	0.98
BBIP1PL3	0	−12.3533	46.0669	44.6343	0.98
BBIP1PL2	0	−12.3504	46.068	44.6354	0.98
BBIP1PL1	0	−12.3389	46.0712	44.6385	0.98
BBIP1L2	0	−4.23185	46.2526	44.824	1.03
BBIP1L1	0	−1.69641	46.2842	44.8578	1.03
BBIP1	0	0	46.3048	44.8797	1.03
BBIP1R1	0	1.69966	46.3256	44.9017	1.03
BBIP1R2	0	4.25111	46.3581	44.9357	1.02
BBIP1PR1	0	12.3472	46.5481	45.1231	0.97
BBIP1PR2	0	12.3554	46.5514	45.1263	0.97
BBIP1PR3	0	12.3572	46.5524	45.1273	0.97
BBIP1PR4	0	12.3579	46.553	45.1278	0.97
BBIP1PR5	0	12.3584	46.5533	45.1281	0.98
BBIP1PR6	0	12.3587	46.5535	45.1283	0.98
BBIP1PR7	0	12.0077	46.5537	45.1285	0.92
BBIP1PR8	0	11.0576	46.5538	45.1286	0.77
BBIP1PR9	0	9.93757	46.554	45.1286	0.59
BBIP1PR10	0	9.27684	46.5541	45.1287	0.49
BBIP1PR11	0	9.2151	46.5543	45.1287	0.47
BBIP1PR12	0	9.51376	46.5544	45.1287	0.52
BBIP1PR13	0	10.2601	46.5545	45.1288	0.63
BBIP1PR14	0	11.849	46.5545	45.1288	0.87
BBIP1PR15	0	14.042	46.5546	45.1289	1.21

C Table of Lie maps of accelerator elements

Table of Lie maps (adapted from Chao[14] Table 4)		
Element	Lie Map	Map
Drift	$e^{:-\frac{1}{2}Lp^2:}$	$x = x_0 + Lp_0$ $p = p_0$
Thin Quad	$e^{:-\frac{1}{2f}x^2:}$	$x = x_0$ $p = p_0 - \frac{1}{f}x_0$
Thin Multipole	$e^{:\lambda x^n:}$	$x = x_0$ $p = p_0 + \lambda n x_0^{n-1}$
Thick focusing Quad	$e^{:-L(kx^2+p^2):}$	$x = x_0 \cos kL + \frac{p_0}{k} \sin kL$ $p = -kx_0 \sin kL + kp_0 \cos kL$
Thick defocusing Quad	$e^{:L(kx^2-p^2):}$	$x = x_0 \cosh kL + \frac{p_0}{k} \sinh kL$ $p = kx_0 \sinh kL + kp_0 \cosh kL$
Coordinate shift	$e^{:ax+bp:}$	$x = x_0 - b$ $p = p_0 + a$
Rotation	$e^{:-\frac{1}{2}\mu(x^2+p^2):}$	$x = x_0 \cos\mu + p_0 \sin\mu$ $p = -x_0 \sin\mu + p_0 \cos\mu$

D Mathematical derivations

D.1 Eigenbasis of harmonic oscillator Lie map

$: \frac{1}{2}(x^2+p^2) :$ generates a rotation. The generator of the one-turn map $e^{:f2:}$ takes this form. Any quadratic Hamiltonian can be brought to this form by completing the square and scaling. Considering $(p+ix)^n$ as candidate eigenfunction

$$\begin{aligned} : \frac{1}{2}(x^2+p^2) : (p+ix)^n &= \frac{\partial \frac{x^2+p^2}{2}}{\partial x}\frac{\partial (p+ix)^n}{\partial p} - \frac{\partial \frac{x^2+p^2}{2}}{\partial p}\frac{\partial (p+ix)^n}{\partial x} \\ &= nx(p+ix)^{n-1} - inp(p+ix)^{n-1} \\ &= -in(p+ix)^n. \end{aligned} \tag{134}$$

$(p+ix)^n$ is indeed an eigenfunction, with eigenvalue $-in$. Similarly $(p-ix)^n$ is an eigenfunction with eigenvalue in. Performing an action-angle transformation (93), these complex polynomials become $\sqrt{2A}^n e^{in\phi}$ and $\sqrt{2A}^n e^{-in\phi}$.

D.2 Lie operators, Lie algebra of operators, and Lie algebra of vector fields

A Lie operator $: H :$ corresponds to vector field X_H (section 4.4.1). Its action on a function f corresponds to the Lie derivative of f along the vector field X_H, $\pounds_{X_H} f$. We will use the simple definition of Lie derivative of a function, the general case is a little more involved.

$$\pounds_{X_H} f = \boldsymbol{\nabla} f \cdot X_H = (\frac{\partial f}{\partial x}, \frac{\partial f}{\partial p}) \cdot (-\frac{\partial H}{\partial p}, \frac{\partial H}{\partial x}) = -\{f, H\} =: H : f. \tag{135}$$

Using the Jacobi Identity of the Poisson bracket

$$\{f,\{g,h\}\} + \{g,\{h,f\}\} + \{h,\{f,g\}\} = 0. \tag{136}$$

This can be rearranged as

$$\{f,\{g,h\}\} - \{g,\{f,h\}\} = \{\{f,g\},h\}. \tag{137}$$

Using Lie operator notation, this becomes

$$: f :: g : h - : g :: f : h = [: f :, : g :]h =: \{f, g\} : h. \tag{138}$$

Then by using (135), by identifying Lie operators as vector fields as done in section 4.4.1, and by defining the action of a vector field on h as $X_S(h) =: S : h$, the previous line can be written as

$$[X_f, X_g](h) = \pounds_{X_{\{f,g\}}}(h). \tag{139}$$

This is also the definition of the Lie derivative of a vector field: $(\pounds_{X_h} X_g)(h) = [X_f, X_g](h)$.

D.3 Over-line transformation

For an aspect ratio $r = \frac{\sigma_y}{\sigma_x}$, the over-line transformation mentioned in section 3.3 is defined as

$$\begin{aligned} &\overline{a}_x = r a_x, \quad \overline{d}_x = d_x, \quad \overline{a}_y = \frac{a_y}{g_r(t)}, \quad \overline{d}_y = \frac{r d_y}{g_r(t)} \\ &g_r(t) = \sqrt{1 + (r^2 - 1)t}. \end{aligned} \tag{140}$$

E Lie operators as the adjoint representation

The adjoint representation of an element x in a Lie group g represents x as a linear operator acting on g via the Lie bracket in g. $x \to Ad_x$, $Ad_x(y) = [x, y]$.

The Lie operator of a function is its adjoint representation in the Poisson bracket Lie algebra of Phase Space Functions. The adjoint representation allows for the writing of formulae such as the BCH(85) in closed form.

In general, the procedure to generate the adjoint representation is what was done in the previous section; by defining a Linear operator Ad_X for any X in the Lie algebra, whose action is defined via the Lie bracket $Ad_x(Y) = \{X, Y\}$. This raises X from vector to operator. The adjoint representation has of course its own adjoint representation which can be constructed using its own Lie bracket, and so on.

The adjoint representation preserves Lie brackets. To show this, let $\{,\}$ denote the Lie bracket of X, Y, and $[,]$ denote the commutator Lie bracket of Ad_X, Ad_Y, consider:

$$\begin{aligned} Ad_{\{X,Y\}}(Z) &= \{\{X, Y\}, Z\} \\ &= (Ad_X Ad_Y - Ad_Y Ad_X)(Z) \\ &= [Ad_X, Ad_Y](Z) \end{aligned} \tag{141}$$

Note that applied to Lie operators, this becomes : $\{f, g\} := [: f :, : g :]$.

Because the bracket is preserved, adjoint representation is isomorphic (equivalent) as Lie algebra when we can assign X to Ad_X in one-to-one correspondence. However, as is the case with the Poisson bracket Lie algebra of phase space functions, this is not always possible. The Poisson bracket does not see constants, so : $f(q, p) + constant :=: f(q, p) :$. Nonetheless, since the mechanics do not depend on constants, those can be ignored in the Poisson bracket Lie algebra; the Lie operators in the adjoint representation effectively form an equivalent Lie algebra in this case; they are isomorphic under the equivalence class of an additive constant (much like anti-derivatives).

F Comparison of Tracking and effective Hamiltonian

The effective Hamiltonian is perturbative in beam-beam impulse strength. In the regime of small impulse with respect to linear betatron motion, it gives an accurate representation of the system. However, when computing the effective Hamiltonian, two truncations are used. A Bessel summation (68) is used to compute the Fourier coefficients. A Fourier summation (107) is then used to compute the effective Hamiltonian. Both of these are infinite series which are truncated during computations.

At large separations (far outside the Strong beam's core), the Bessel summation needs not many terms and converges rapidly. However, at small separations, this is not true.

The required upper bound for the Fourier series is determined by the system's working point and neighbouring resonances. For working point analyzed in this thesis (62.31,60.32), the inclusion of 16th order resonances cause the tracking and invariant to agree within 0.05 %.

For the following figures (20, 21), a percent deviation of the effective Hamiltonian from tracking in X was calculated, and averaged over the phase ϕ_x, and plotted for different values of upper bounds for Bessel and Fourier sums. The beam-beam setup is the simplified 2IR long-range/head-on combined model used in figure 11.

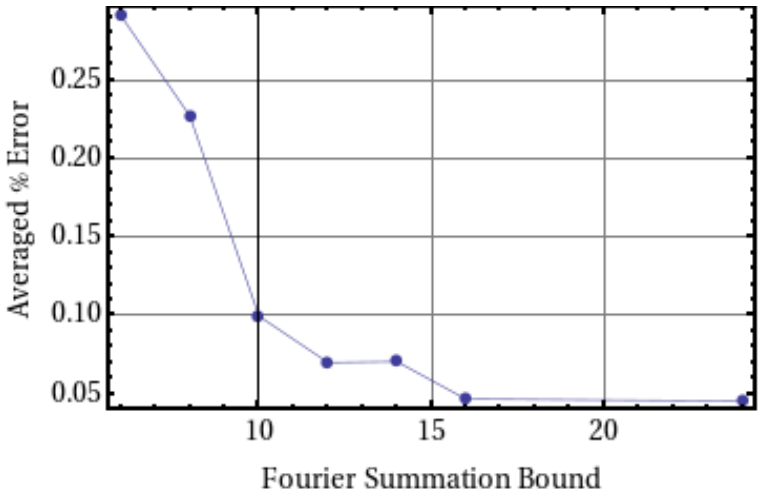

Figure 20: Averaged percent error of Invariant from Tracking in X for different Fourier Bounds, (Bessel Bound=20), Separation=12.5 σ

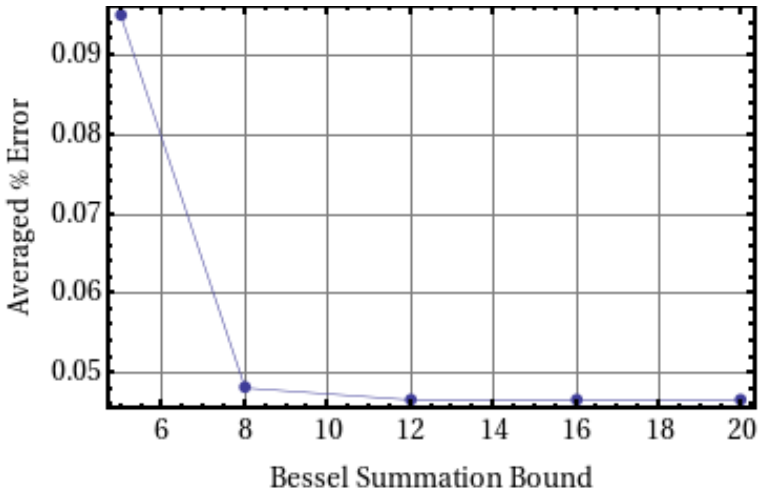

Figure 21: Averaged percent error of Invariant from Tracking in X for different Bessel Bounds, (Fourier Bound=16), Separation=12.5 σ

For a lower separation 9 σ, the Bessel sum converges more slowly. The tracking vs invariant show a visual disagreement. Figure 22 show the averaged % error for different Bessel upper bounds at a separation of 9 σ, which converges slower than at a separation of 12.5 σ, to a value of approximately 0.05 %. It seems likely this the accuracy of the perturbative regime; the % error can only be decreased further by decreasing the beam-beam strength.

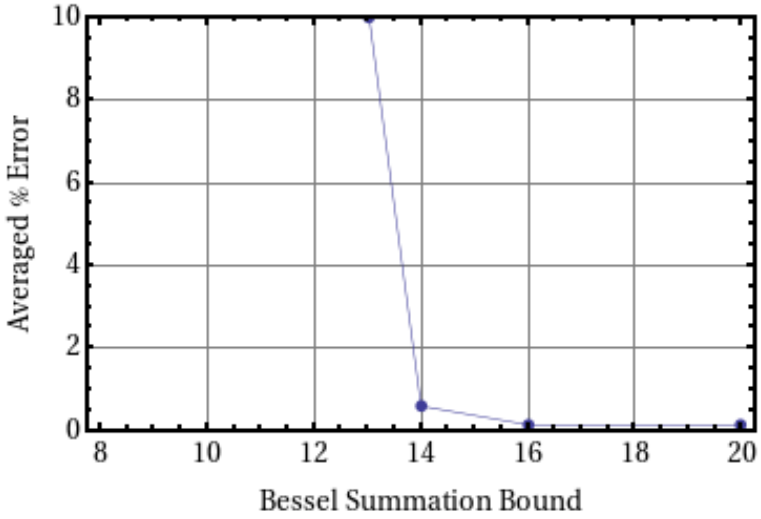

Figure 22: Averaged percent error of Invariant from Tracking in X for different Bessel Bounds, (Fourier Bound=16), Separation=9 σ

Omitted figures

Simple toy model consisting of 2 head-on interactions, 10th order long-range resonance cancelling Width function

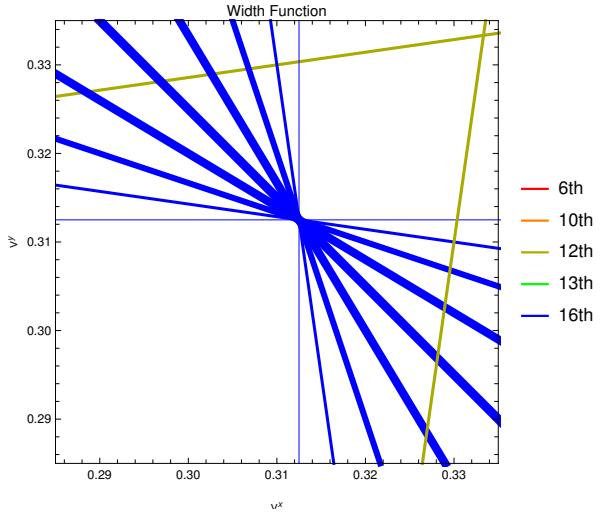

(a) Resonances order 10,12,13,16 $\frac{\pi}{2}$ phasing

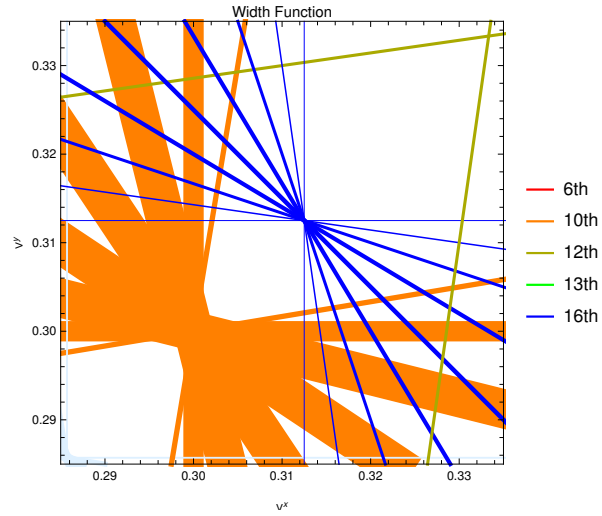

(b) Resonances order 10,12,13,16 at $\frac{2\pi}{3}$ phasing

Figure G.23: Simple toy model 10th order resonance cancelling of head-on BB Width function: 10th order(orange), 12th order(dark green), 16th order(blue)

2 IR realistic simplified model 10th order resonance cancelling

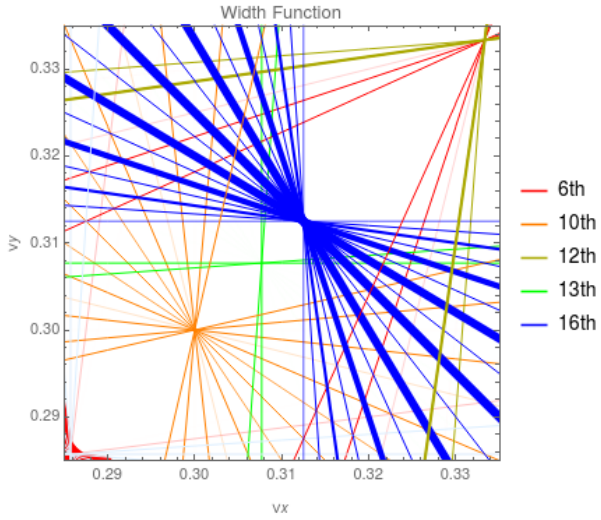

(a) Resonances order $5-16$ at 64.5π phasing

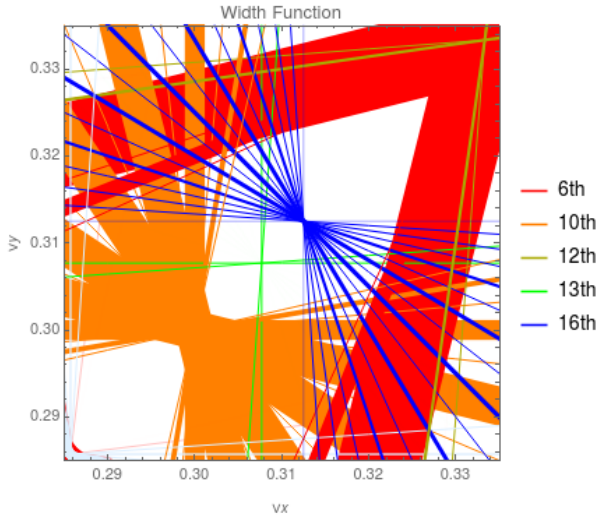

(b) Resonances order $5-16$ at $64+2/3\pi$ phasing

Figure G.24: 2 IR realistic simplified model 10th order resonance cancelling: 6th order(red), 10th order(orange), 13th order(green), 16th order(blue)

70 impulse IR1-IR5 model 10th order (orange) resonance cancellation by the phasing of 2 IRs Width function plot: phasing tolerance test

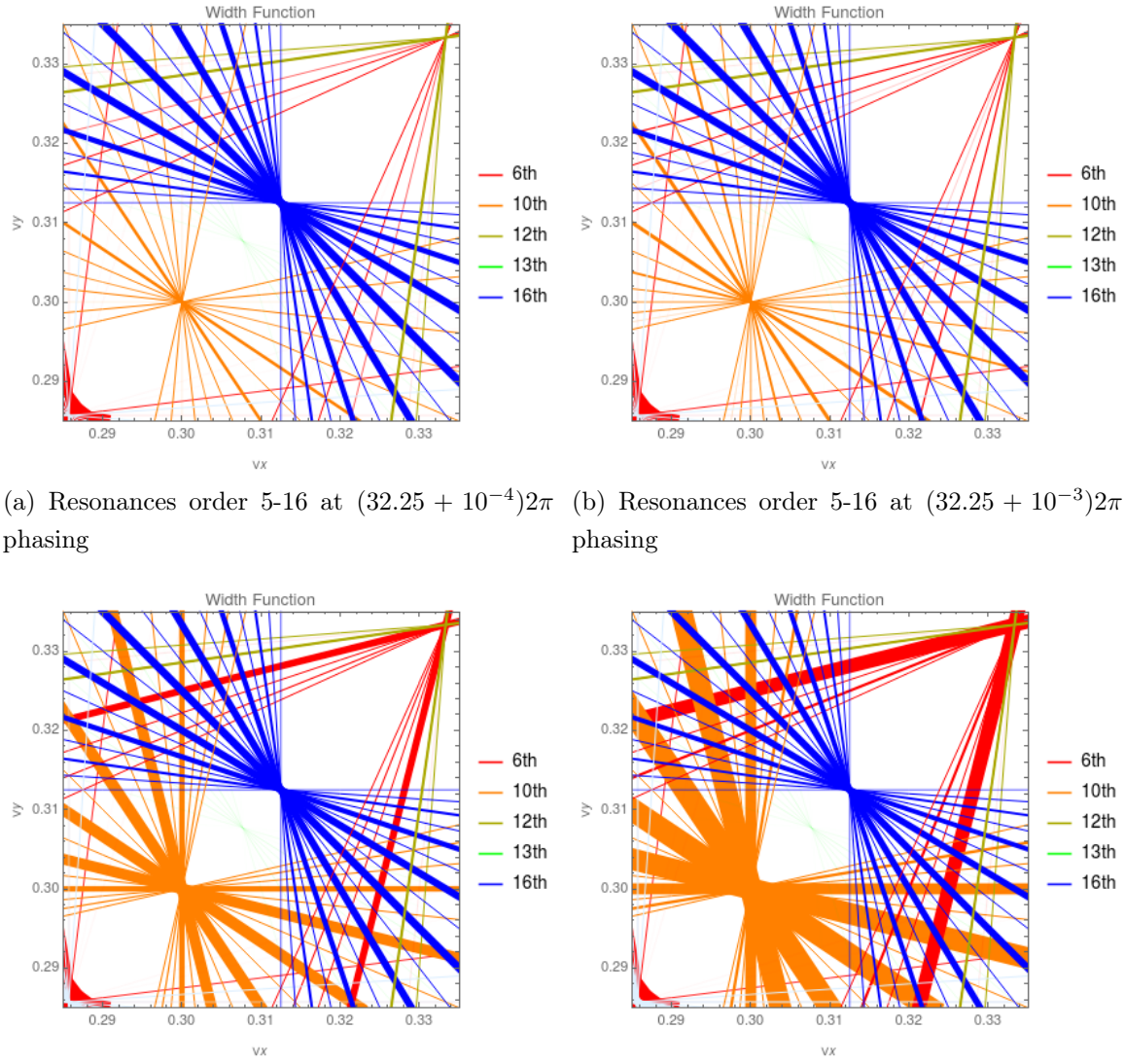

(a) Resonances order 5-16 at $(32.25 + 10^{-4})2\pi$ phasing

(b) Resonances order 5-16 at $(32.25 + 10^{-3})2\pi$ phasing

(c) Resonances order 5-16 at $(32.25 + 5 * 10^{-3})2\pi$ phasing

(d) Resonances order 5-16 at $(32.25 + 10^{-2})2\pi$ phasing

Figure G.25: 70 impulse IR1-IR5 model 10th order (orange) resonance cancellation by the phasing of 2 IRs Width function plot: 6th order(red), 10th order(orange), 13th order(green), 16th order(blue).

70 impulse IR1-IR5 model 10th order resonance cancellation tolerance by the phasing of 2 IRs invariant plot: tolerance test

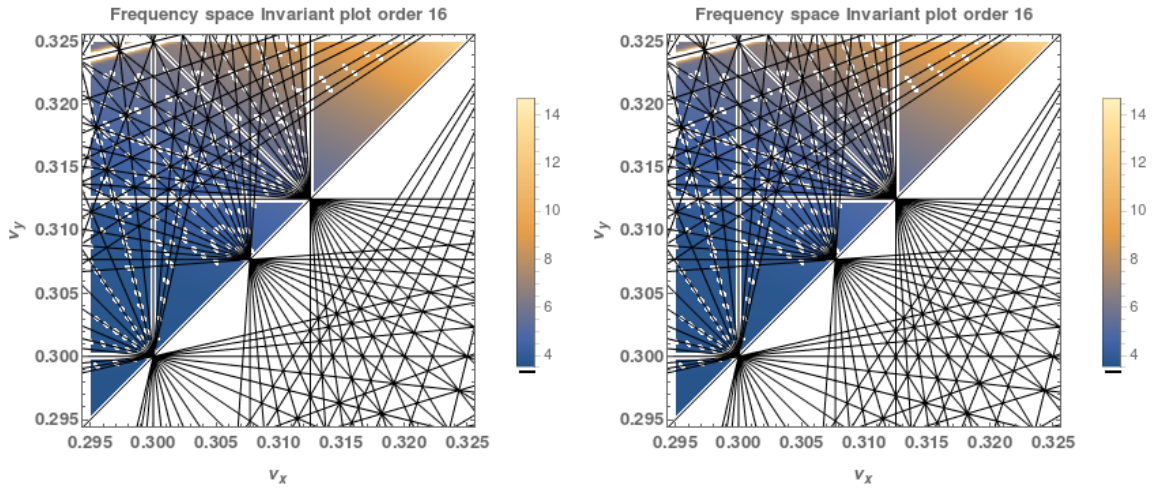

(a) Resonances order 5-16 at $(32.25 + 10^{-4})2\pi$ phasing

(b) Resonances order 5-16 at $(32.25 + 10^{-3})2\pi$ phasing

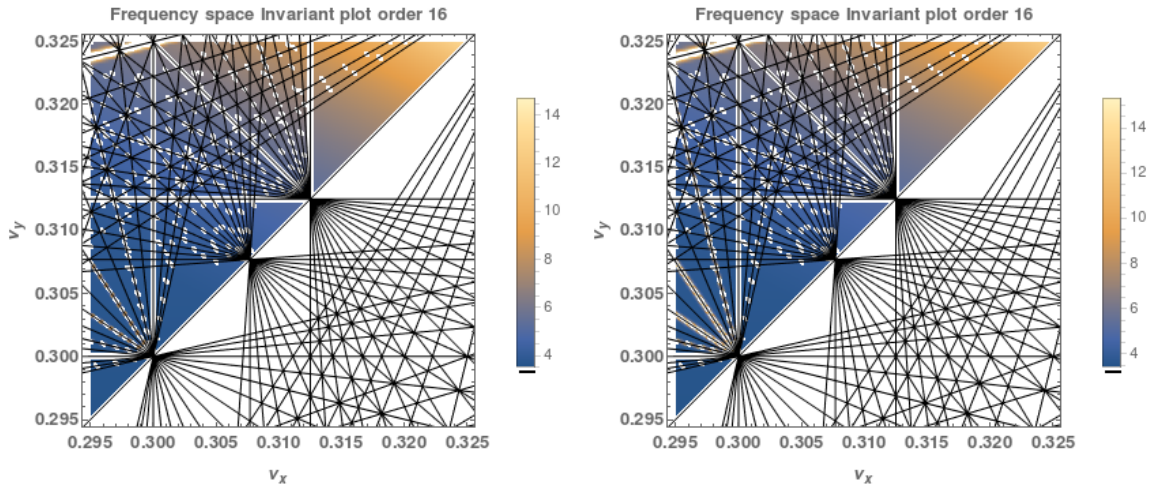

(c) Resonances order 5-16 at $(32.25 + 5 * 10^{-3})2\pi$ phasing

(d) Resonances order 5-16 at $(32.25 + 10^{-2})2\pi$ phasing

Figure G.26: 70 impulse IR1-IR5 model 10th order resonance near cancellation from phasing of 2 IRs invariant plot. Scales in $[\sigma^2]$.

70 impulse IR1-IR5 model invariant plot with varying crossing angles

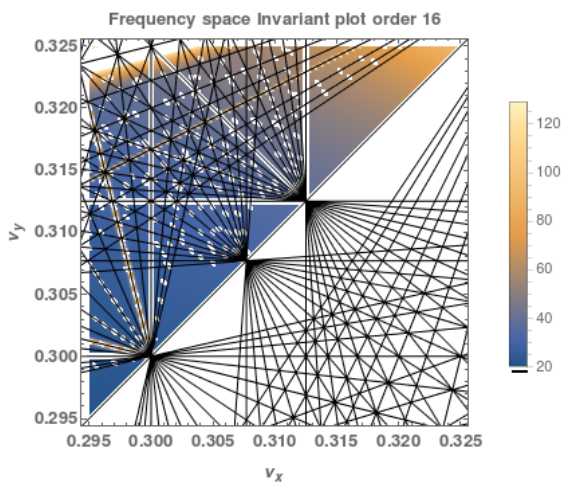

(a) 2 IR HL-LHC ($\frac{1}{2}590 = 295$) μrad crossing angle

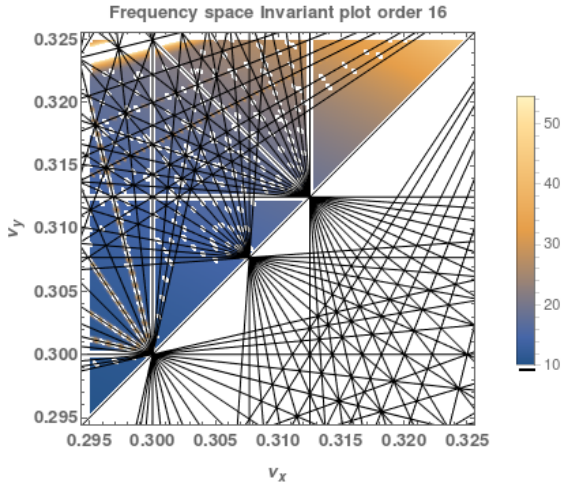

(b) 2 IR HL-LHC ($\frac{2}{3}590 \approx 393$) μrad crossing angle

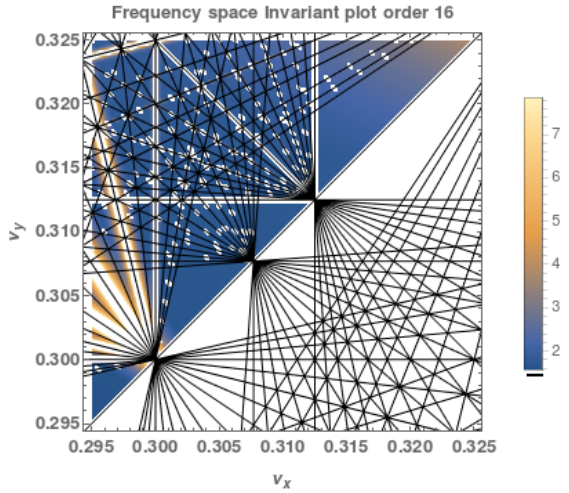

(c) 2 IR HL-LHC ($\frac{3}{2}590 = 885$) μrad crossing angle

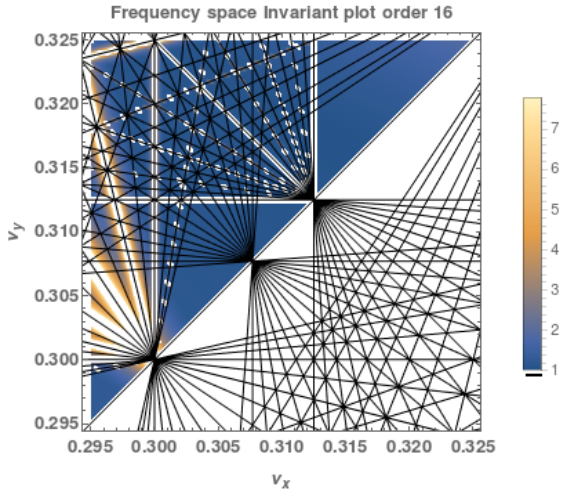

(d) 2 IR HL-LHC ($3 * 590 = 1770$) μrad crossing angle

Figure G.27: 70 impulse IR1-IR5 model invariant plot with varying crossing angles. Scales in $[\sigma^2]$.

70 impulse IR1-IR5 model invariant plot near working point (0.475,0.485)

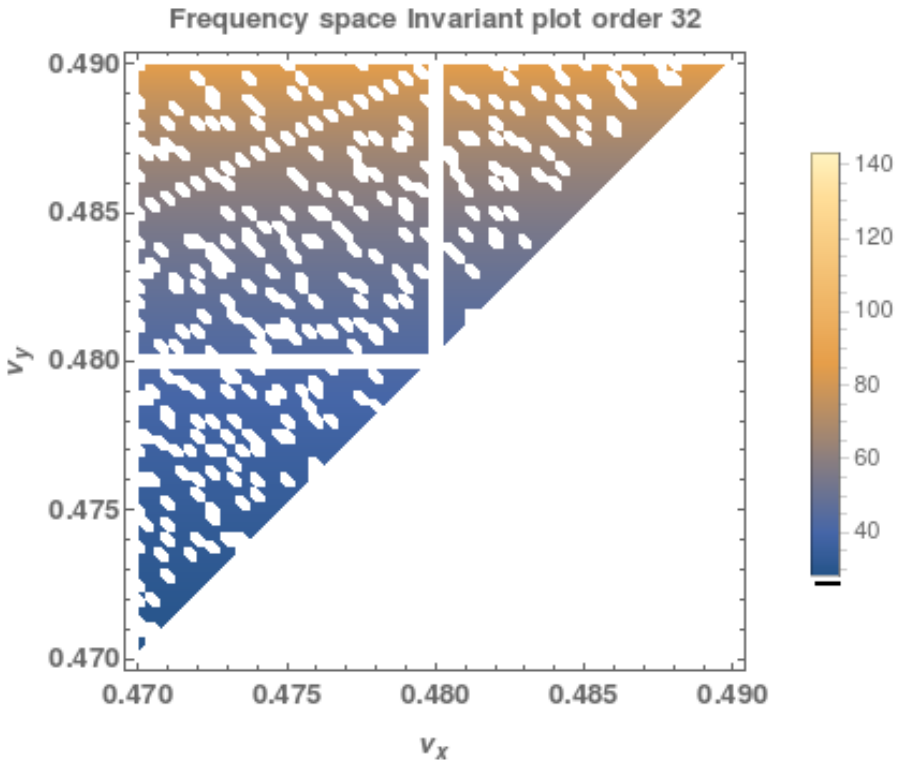

Figure G.28: 70 impulse IR1-IR5 model, invariant plot near working point (0.475,0.485). Scales in $[\sigma^2]$.

.

Normalized(a_x^2) Action-angle plots of Tracking(blue dots) vs Invariant(red lines) of alternate working point (0.475,0.485)

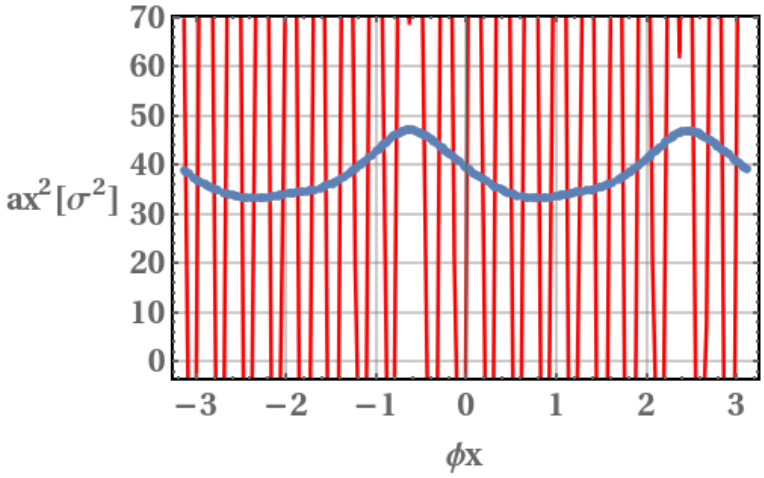

Figure G.29: $X - P_x$ plane Action-Angle plot of Tracking(blue dots) vs Invariant (red lines)

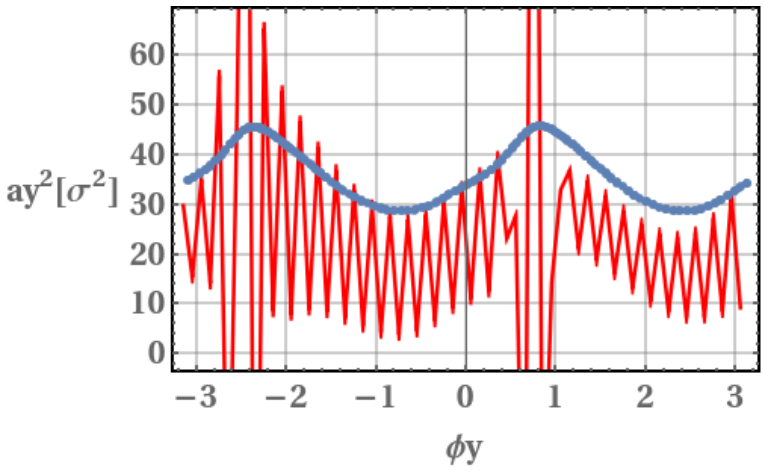

Figure G.30: $Y - P_y$ plane Action-Angle plot of Tracking(blue dots) vs Invariant (red lines)